frontiers | Frontiers in Cell and Developmental Biology

TYPE Original Research
PUBLISHED 10 August 2023
DOI 10.3389/fcell.2023.1178992

OPEN ACCESS

EDITED BY
Adelaide Fernandes,
University of Lisbon, Portugal

REVIEWED BY
Leslie Climer,
St. Jude Children's Research Hospital, United States
Wallace B. Thoreson,
University of Nebraska Medical Center, United States

*CORRESPONDENCE
Susann Michanski,
susann.michanski@med.uni-goettingen.de
Carolin Wichmann,
carolin.wichmann@med.uni-goettingen.de

RECEIVED 03 March 2023
ACCEPTED 17 July 2023
PUBLISHED 10 August 2023

CITATION
Michanski S, Henneck T, Mukhopadhyay M, Steyer AM, Gonzalez PA, Grewe K, Ilgen P, Gültas M, Fornasiero EF, Jakobs S, Möbius W, Vogl C, Pangršič T, Rizzoli SO and Wichmann C (2023), Age-dependent structural reorganization of utricular ribbon synapses.
Front. Cell Dev. Biol. 11:1178992.
doi: 10.3389/fcell.2023.1178992

Age-dependent structural reorganization of utricular ribbon synapses

Susann Michanski[1,2,3]*, Timo Henneck[4], Mohona Mukhopadhyay[5], Anna M. Steyer[6,7], Paola Agüi Gonzalez[8], Katharina Grewe[8], Peter Ilgen[9,10,11], Mehmet Gültas[12], Eugenio F. Fornasiero[8], Stefan Jakobs[9,10,11], Wiebke Möbius[3,6], Christian Vogl[2,13,14], Tina Pangršič[2,3,5], Silvio O. Rizzoli[8] and Carolin Wichmann[1,2,3]*

[1]Molecular Architecture of Synapses Group, Institute for Auditory Neuroscience, InnerEarLab and Center for Biostructural Imaging of Neurodegeneration, University Medical Center Göttingen, Göttingen, Germany, [2]Collaborative Research Center 889, University of Göttingen, Göttingen, Germany, [3]Multiscale Bioimaging Cluster of Excellence (MBExC), University of Göttingen, Göttingen, Germany, [4]Biology Bachelor Program, University of Göttingen, Göttingen, Germany, [5]Experimental Otology Group, InnerEarLab, Department of Otolaryngology, Institute for Auditory Neuroscience, University Medical Center Göttingen, Göttingen, Germany, [6]Electron Microscopy-City Campus, Department of Neurogenetics, Max Planck Institute for Multidisciplinary Sciences, Göttingen, Germany, [7]Center Nanoscale Microscopy and Molecular Physiology of the Brain (CNMPB), University of Göttingen, Göttingen, Germany, [8]Department for Neuro-and Sensory Physiology, University Medical Center Göttingen, Center for Biostructural Imaging of Neurodegeneration (BIN), Göttingen, Germany, [9]Clinic of Neurology, University Medical Center Göttingen, Göttingen, Germany, [10]Department of NanoBiophotonics, Max Planck Institute for Multidisciplinary Sciences, Göttingen, Germany, [11]Fraunhofer Institute for Translational Medicine and Pharmacology ITMP, Translational Neuroinflammation and Automated Microscopy TNM, Göttingen, Germany, [12]Faculty of Agriculture, South Westphalia University of Applied Sciences, Soest, Germany, [13]Presynaptogenesis and Intracellular Transport in Hair Cells Group, Institute for Auditory Neuroscience and InnerEarLab, University Medical Center Göttingen, Göttingen, Germany, [14]Auditory Neuroscience Group, Institute of Physiology, Medical University Innsbruck, Innsbruck, Austria

In mammals, spatial orientation is synaptically-encoded by sensory hair cells of the vestibular labyrinth. Vestibular hair cells (VHCs) harbor synaptic ribbons at their presynaptic active zones (AZs), which play a critical role in molecular scaffolding and facilitate synaptic release and vesicular replenishment. With advancing age, the prevalence of vestibular deficits increases; yet, the underlying mechanisms are not well understood and the possible accompanying morphological changes in the VHC synapses have not yet been systematically examined. We investigated the effects of maturation and aging on the ultrastructure of the ribbon-type AZs in murine utricles using various electron microscopic techniques and combined them with confocal and super-resolution light microscopy as well as metabolic imaging up to 1 year of age. In older animals, we detected predominantly in type I VHCs the formation of floating ribbon clusters, mostly consisting of newly synthesized ribbon material. Our findings suggest that VHC ribbon-type AZs undergo dramatic structural alterations upon aging.

KEYWORDS

aging, ribbon synapse, synaptogenesis, utricle, vestibular hair cells

Introduction

Sensory receptor cells in the eye and inner ear are equipped with specialized presynaptic organelles—synaptic ribbons—that tether dozens to hundreds of synaptic vesicles (SVs). This system enables indefatigable quantal release of the neurotransmitter glutamate (Sterling and Matthews, 2005; Moser et al., 2006; Matthews and Fuchs, 2010; Rutherford and Moser, 2016; Moser et al., 2019).

The mammalian vestibular system contains multiple sensory organs, the utricle and the saccule for sensing of linear acceleration and gravity, and the ampullae in the semicircular canals for the detection of head rotation (Li et al., 2016). Each of the vestibular organs harbors a sensory epithelium carrying two types of vestibular hair cells (VHCs) (Wersall, 1956). Ribbons decorate the active zones (AZs) of both, calyceal synapses of type I as well as conventional bouton synapses of type II VHCs. Morphologically, vestibular ribbons are highly variable in size, shape and number depending on the species, hair cell type and location (Eatock and Lysakowski, 2006). However, in comparison to auditory and visual ribbon synapses, relatively little is known about the synaptic architecture of vestibular ribbon synapses. Since the decline of vestibular function starts already at the age of 40 (Agrawal et al., 2009; Bermúdez Rey et al., 2016) and vestibular deficits can significantly impair the quality of life of affected patients, detailed longitudinal analyses of VHC ultrastructure upon maturation and aging are essential, but to date surprisingly scarce.

As evident by decreased amplitudes alongside increased latencies and thresholds of ocular vestibular-evoked myogenic potentials (oVEMPs) in humans (Iwasaki et al., 2008; Piker et al., 2011; Rosengren et al., 2011; Agrawal et al., 2012), vestibular function declines with age. This is in line with the observation of increased occurrences of vertigo, recurrent dizziness, nausea, disorientation, blurred vision, imbalance, and increased risk of falling in the elderly (Neuhauser et al., 2005; Neuhauser, 2007; Agrawal et al., 2012). In this context, it remains to be clarified, which cells or subcellular structures undergo age-related deterioration in the utricular system as well as other vestibular organs.

As suggested by several studies in rodent cochlear hair cells, ribbon synapse abundance, size and shape are connected to functional changes (Sobkowicz et al., 1982; Sobkowicz et al., 1986; Stamataki et al., 2006; Wong et al., 2014; Michanski et al., 2019; Peineau et al., 2021), as well as the morphology of AZ-proximal mitochondria (Stamataki et al., 2006). Furthermore, ribbon synapse dysfunction or degeneration appear to present major factors underlying age-related hearing loss (Stamataki et al., 2006; Huang et al., 2012; Wong et al., 2014; Peineau et al., 2021). Whether a similar correlation exists in VHCs is largely unknown, but it is tempting to speculate that disruption of the presynaptic energy supply, for example during aging, may negatively influence synaptic performance. Mitochondria are important for energy supply and Ca^{2+} buffering at synapses and thus play a prominent role in neuronal homeostasis (Devine and Kittler, 2018). Moreover, recent work in zebrafish lateral line neuromast hair cells indicated an important role of synaptic mitochondria in ribbon size regulation during development and synaptic function as well as structural integrity upon maturation (Wong et al., 2019).

Therefore, we set out to analyze the impact of maturation and aging on the murine utricular VHC synapses by quantifying various aspects of presynaptic AZ structure at ages ranging from 1 week to 11 months and beyond. To do so, we combined transmission electron microscopy (TEM) with nanoscale secondary ion mass spectrometry (NanoSIMS), electron tomography, focused ion beam-scanning electron microscopy (FIB-SEM) as well as confocal and stimulated emission depletion (STED) microscopy.

We found that, while AZs of both types of VHCs contained ribbons of various shapes and sizes, type I VHCs were dominated by elongated ribbons upon maturation. Moreover, type I VHCs progressively formed complex cytosolic ribbon clusters that often were void of any physical contact to the AZ membrane along with enlarged mitochondria. In contrast to previous reports describing such ribbon clusters in VHCs (Favre et al., 1986; Park et al., 1987; Woods and Park, 1987; Sans and Scarfone, 1996), we now combined a detailed presynaptic morphometric analysis with isotopic labeling to additionally establish ribbon turnover rates in elderly VHCs. This analysis revealed that floating ribbons seem to be newly-synthesized in comparison to attached ribbons, while both ribbon populations appeared much "younger" than other VHC organelles such as mitochondria. In contrast, type II VHCs showed a relatively stable AZ architecture with comparable ribbon counts and shapes, as well as mitochondrial sizes independent of aging.

In summary, our data suggests that the presynaptic architecture of VHCs—in particular in type I VHCs—retains its ability to undergo active morphological changes in adult stages. Our findings support the hypothesis that new VHC ribbons are continuously formed, but fail to attach at the presynaptic AZ and hence accumulate in its proximity. Forming clusters, they could serve as a reserve pool of ribbons when needed, or alternatively, may represent pathological accumulation of ribbons rendered incapable of attaching at the presynaptic membrane.

Results

Upon maturation, the number of membrane-attached synaptic ribbons per presynaptic AZ decreases

To investigate maturation and aging of utricular VHC ribbon synapses, we performed a detailed ultrastructural analysis of type I and type II VHCs in mice of five age groups (postnatal day (P)9, P15, P20, 3 months, and 9–11 months). This covered the developmental period of synaptogenesis, through maturation and ultimately to the beginning of a functional decline. Behavioral studies of balance reflexes in rats revealed that the vestibular system is functionally mature around P16 (Hård and Larsson, 1975; Lannou et al., 1979) and during the first two postnatal weeks, the VHCs gradually acquire mature ionic conductances (Rüsch et al., 1998). However, data from detailed physiological and morphological examinations of rodents suggest that VHC synaptic connectivity does not reach a fully mature state until 3–4 weeks of age (Curthoys, 1979; Nordemar, 1983; Dechesne et al., 1986; Kawamura et al., 1998; Jamon, 2014). In order to distinguish between type I and II VHCs in immature P9 animals (with not yet fully developed calyces), only

10.3389/fcell.2023.1178992

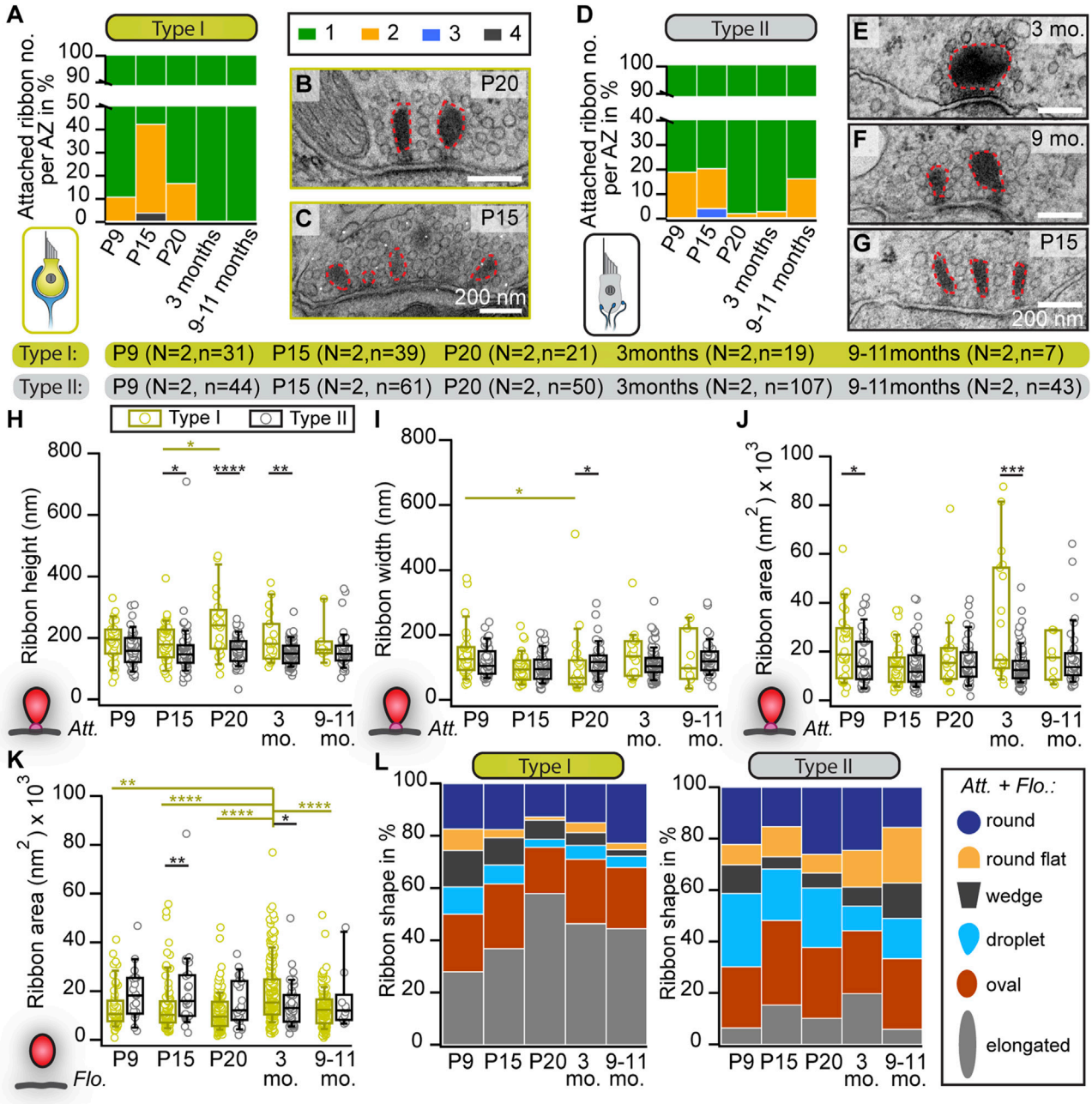

FIGURE 1
Changes in the abundance and shape of VHC ribbons upon maturation and aging. **(A,D)** Analysis of the number of membrane-attached synaptic ribbons reveals a larger proportion of multiple ribbons per AZ in immature type I **(A)** and type II **(D)** VHCs compared to mature ages. N = number of animals, n = number of membrane-attached ribbons. **(B,C,E–G)** Examples of electron micrographs depicting either multiple or single synaptic ribbons (highlighted with red dashed lines) in type I **(B,C)** and type II **(E–G)** VHCs. **(H–K)** Box plots show random section quantifications of the ribbon size measurements for all age groups of attached (*Att.*; **(H–J)**) and floating ribbons (*Flo.*; **(K)**). No prominent changes regarding the ribbon area, height, and width could be observed in older animals. **(L)** Proportion of ribbons (including attached and floating ribbons) categorized into different types of shapes, respectively for all quantified ages. Significant differences between two groups were analyzed with a two-tailed *t*-test or Mann–Whitney Wilcoxon test. For multiple comparisons, ANOVA followed by the *post hoc* Tukey or Kruskal-Wallis (KW) test followed by NPMC test was performed. For more detailed information, including n values for floating ribbons, see also Supplementary Table S2.

VHCs with clearly identifiable surrounding calyx or afferent bouton contacts were considered for analysis.

We first analyzed AZs of conventionally-embedded utricles that contain ribbons with clear attachments via a presynaptic density (PD) to the AZ membrane. In random 2D ultrathin sections, we determined the abundance, shape, and size of membrane-attached ribbons, analogous to our previous study on cochlear inner hair cells (IHCs) (Michanski et al., 2019). In young VHCs of both types, we frequently found more than one ribbon per AZ (Figures 1A–G), whereas, in VHCs of adults,

10.3389/fcell.2023.1178992

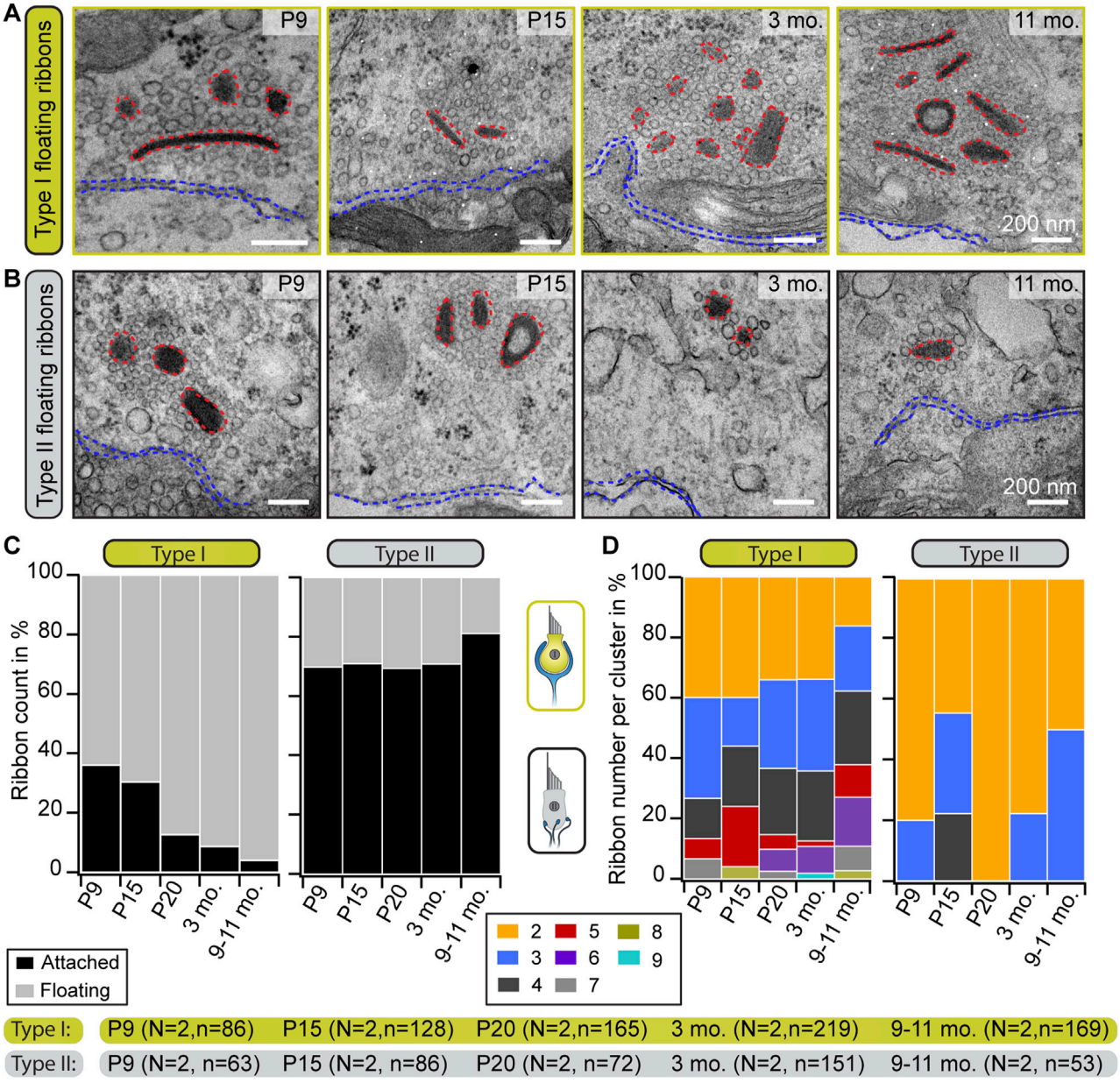

FIGURE 2
Progressive accumulation of floating ribbons in type I VHCs. **(A,B)** Representative electron micrographs showing single and multiple floating ribbons (red dashed lines) in type I **(A)** and type II **(B)** VHCs. All depicted ribbons appear to lack the presynaptic contact to the HC membrane (blue dashed lines). **(C)** Graphs representing the proportions of floating and membrane-attached ribbons during maturation and aging. Mature type I VHCs possess predominantly floating ribbons, whereas type II VHCs exhibit mainly attached ribbons throughout all investigated ages. **(D)** Quantification of the total number of ribbons per cluster reveals the occurrence of large ribbon clusters in both VHC types. With advancing age, the ribbon count per cluster increases in type I VHCs but slightly decreases in type II VHCs. N, number of animals; n, number of ribbons (including membrane-attached and floating ribbons).

typically, a single ribbon was attached at the AZ plasma membrane (Figures 1A, D). Our 2D TEM data further revealed remarkably stable and largely comparable mean synaptic ribbon areas in the membrane-attached ribbon populations of type I and type II VHCs as well as between the different age groups (for quantification parameters see materials and methods; Supplementary Figure S1A). Nevertheless, there was a trend of type I VHC ribbons towards enlarged heights across all age groups in comparison to type II VHC ribbons (Figures 1H–J; Supplementary Table S1).

To our surprise, in contrast to mature auditory IHCs, we observed several "floating" synaptic ribbons—defined as ribbons lacking any apparent contact with the plasma membrane in the 2D image—throughout all age groups and in both VHC types (Supplementary Figures S1B, C; Supplementary Table S3). While no major systematic differences in floating ribbon size could be

observed in either VHC type or between age groups, floating ribbons from 3-month-old type I VHCs displayed significantly larger ribbon areas in comparison to type I VHCs in other age groups (Figure 1K; Supplementary Table S1). Additionally, we categorized synaptic ribbon shapes (Figure 1L), since it is well established in auditory IHCs that ribbon morphology changes drastically from rather round shapes prior to hearing onset to elongated and droplet-shaped ribbons in adulthood (Sobkowicz et al., 1982; Wong et al., 2014; Michanski et al., 2019). In VHCs, ribbon size and shape have been found to vary depending on the species, VHC type, developmental stage, vestibular organ and the zonal region of the epithelium (Eatock and Lysakowski, 2006). Interestingly, our analysis revealed that upon maturation, type I VHCs of the utricle displayed an apparent increase in the abundance of elongated ribbons (on the expense of droplet, wedge and round-flat ribbons), which goes along with the observation of enlarged ribbon heights in type I VHCs. Conversely, ribbon shape distributions in type II VHCs remained with some variability much more uniform across different ages (Figure 1L; Supplementary Table S2).

Progressive increase in the number of floating ribbons and ribbon cluster formation in type I VHCs

A characteristic feature of immaturity in cochlear IHCs is the presence of round, free-floating ribbon precursors, which attach to the AZ membrane or might fuse with membrane-anchored ribbons during maturation (Sobkowicz et al., 1982; Wong et al., 2014; Michanski et al., 2019). Conversely, floating ribbons appear to persist in VHCs independent of their developmental stage (Figures 2A, B).

To now further characterize these organelles in greater detail in both VHC types, a range of different ultrastructural approaches was employed. In 2D random sections, we observed that, while the fraction of floating ribbons in type I VHCs dramatically increased with age—ultimately constituting ~95% of all AZ-proximal ribbons in the 9–11 months age group—(Figure 2C; Supplementary Table S3), the proportion of floating ribbons in type II VHCs remained remarkably stable at ~20–30%. When measuring the nearest distance between these floating ribbons and the plasma membrane, we found appositions predominantly ~200 nm from the AZ membrane, with generally tighter spacing in type II VHCs for almost all age groups (Supplementary Figure S1D; Supplementary Table S8). This finding may be indicative of a progressive age-dependent anchoring deficit—especially in type I VHCs.

These floating ribbons then further accumulated into clusters (≥2 ribbons) with increasing complexity and often—but not always—resided in direct proximity to membrane-attached ribbons at the AZs of both VHC types. In type I VHCs, such clusters were composed of up to nine ribbons (Figures 2A, D; Supplementary Figure S1C), whereas a maximum of four—but mostly a pair of ribbons per cluster—were observed in type II VHCs analyzed from random sections (Figures 2B, D; Supplementary Table S3). In type I VHCs, the ribbon clusters grew continuously from P20 onwards, while a similar trend was not observed in type II VHCs. There, we even detected a decrease of cluster ribbon content at P20 followed by a slight increase at older ages (Figure 2D). A striking increase in the proportion of single ribbons was observed in type II VHCs, whereas in type I VHCs, synaptic ribbons in clusters clearly dominated at older ages (Supplementary Figure S1E; Supplementary Table S3).

Since floating and attached ribbons alike exhibited a translucent core in some cases (Figures 2A, B; Supplementary Figure S1C), we quantified the frequency of occurrence of this phenomenon. This special ribbon morphology has previously been described in several vestibular and cochlear studies, but mostly in adult tissues (Engström et al., 1972; Favre and Sans, 1979; Sjöbäck and Gulley, 1979; Liberman, 1980; Sobkowicz et al., 1982; Park et al., 1987; Woods and Park, 1987; Lysakowski, 1996; Lysakowski and Goldberg, 1997; Stamataki et al., 2006; Lysakowski and Goldberg, 2008; Michanski et al., 2019). For cochlear ribbons, it has been proposed that this feature appearing in adult mice might indicate 'old' ribbons that reached their life span prior to their degradation (Sobkowicz et al., 1982). Yet, in the present study on VHCs, evaluation of floating and attached VHC ribbon counts with a translucent core revealed no age-dependent increase in this ribbon feature (Supplementary Figure S1F). Therefore, we hypothesize that ribbon size—but not structural "age"—determines the formation of a translucent core.

Since the nature of 2D-analysis, which is relying on single ultrathin sections, may lead to a systematic under-estimation of ribbon attachment, we next verified the abundance of free-floating ribbons and their accumulation in larger clusters, by performing electron tomography. This 3D approach confirmed the occurrence of ribbon clusters consisting either of exclusively floating ribbons (Movie 1) or floating together with some membrane-attached ribbons (Movie 2), predominantly in type I VHCs vs. mainly attached single ribbons in mature type II VHCs (Movie 3).

Movie 1–3: electron tomography with 3D segmentation of ribbon cluster and single attached ribbons

Tomograms and their corresponding 3D models of mature (3 months) type I/II VHCs depicting several disc-shaped floating ribbons in type I VHCs and typical single attached ribbons in type II VHCs. The different SV pools, membrane-proximal (MP)-SVs and ribbon-associated (RA)-SVs, are defined as displayed in Supplementary Figure S1A.

Red: ribbon, magenta: presynaptic density, dark blue: postsynaptic density, light blue: HC membrane, yellow: SVs, orange: MP-SVs, green: RA-SVs, brown: SV not associated with the ribbon but part of the cluster "cloud". Scale bars: 200 nm.

Movie 1 in Supplementary Presentation S1
Movie 2 in Supplementary Presentation S1
Movie 3 in Supplementary Presentation S1

To exclude the possibility that the preparation method of the delicate tissue could have caused putative artifacts leading to a higher frequency of floating ribbons, we applied an alternative sample preparation method. Here, slow fixative perfusion of the inner ear followed by utricle dissection yielded similar results as with

10.3389/fcell.2023.1178992

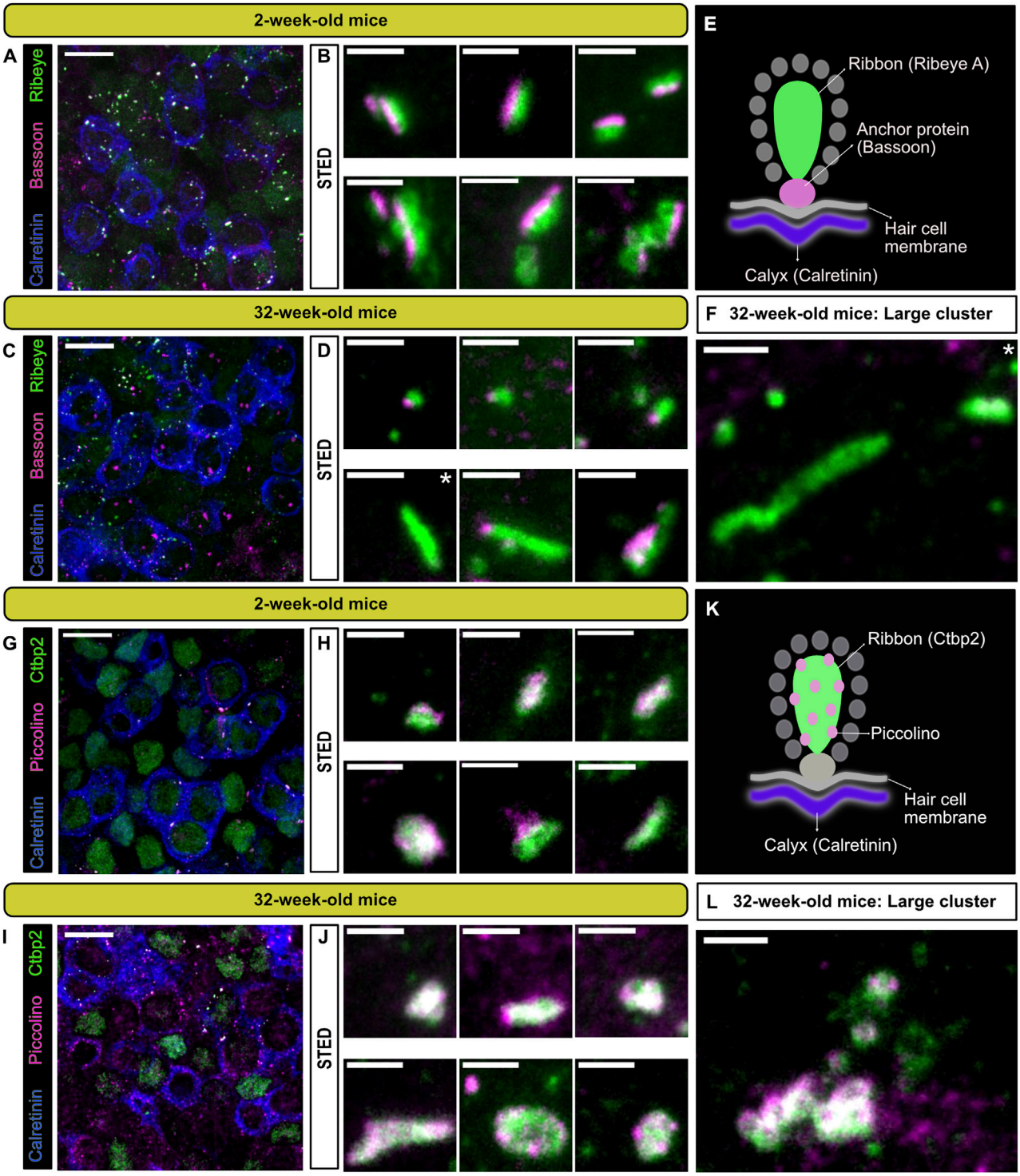

FIGURE 3
Localization of the presynaptic AZ proteins bassoon and piccolino at type I VHCs ribbon synapses. **(A,C,G,I)** 100x confocal images of the utricular striola, identified here by the presence of calretinin (blue) stained single and complex calyces, with combinations of various synaptic proteins. Ribbon proteins RIBEYE A **(A,C)** and CtBP2 **(G,I)** shown in green. Anchoring protein bassoon **(B,D)** and ribbon-associated protein piccolino **(G,I)** shown in magenta. Scale bars in **(A,C,G,I)**: 10 µm. **(B,D,H,J)** Top panels show representative STED images of putative single ribbons or small ribbon clusters and lower panels show images of complex clusters near the type I VHC membranes, with the respective antibody combinations (scale bars for STED images: 1 µm). **(E,K)** Schematic representation of the antibody combinations used for each panel in young (2 weeks) and old mice (32 weeks). **(F,L)** Representative STED images of particularly large ribbon clusters (scale bar: 1 µm). N = 3 animals for each combination. Note that 100x confocal images represent maximal projections of only a few optical planes for better visibility. White asterisks mark the panels depicting ribbons that seemingly lack bassoon (even in the optical planes that were omitted from projections).

our standard preparation method. Moreover, the previously reported age-related progressive genetic hearing loss in C57BL/6J mice (Mikaelian et al., 1974; Henry and Chole, 1980; Shnerson and Pujol, 1981; Willott, 1986; Li and Borg, 1991; Johnson et al., 1997; White et al., 2000; Hequembourg and Liberman, 2001; Ison and Allen, 2003) due to Cdh23 mutation, did not strongly affect vestibular function and morphology does not seem to be altered (Mock et al., 2016). Nevertheless, to exclude the possibility of mouse background related structural changes in VHCs, we further examined utricles of adult (6-month-old) CBA/J wild-type mice. These mice maintain relatively normal hearing until they reach senescence (Willott, 1986; Willott et al., 1988a; Willott et al., 1988b; Shone et al., 1991; Walton et al., 1995; Spongr et al., 1997). Electron micrographs of random and serial sections from CBA/J mice confirmed the frequent abundance of floating ribbons as well as the presence of complex ribbon clusters in type I VHCs of adult mice (Supplementary Figure S2).

Molecular constituents of ribbon clusters

The extremely high percentages of cytoplasmically floating ribbons—especially in type I VHCs (~90% already at P20; Figure 2C)—led to the question whether floating and membrane-attached ribbons in type I and II VHCs are different in their molecular composition from attached ribbons in other HC types. For example, in cochlear IHCs, it could previously be shown that genetic loss of the large structural scaffold bassoon prevented adequate ribbon anchoring at the AZ membrane (Khimich et al., 2005), which was also the case for photoreceptor ribbons (Dick et al., 2003). Therefore, immunohistochemical stainings of the main ribbon components RIBEYE and piccolino as well as the molecular anchor bassoon were performed in order to determine the localization of these proteins. Utilizing confocal and STED microscopy, we detected piccolino on floating ribbons as well as membrane-attached ribbons being part of a ribbon cluster in both VHC types (Figure 3). A qualitative assessment of the images suggested the presence of clusters in both young and older animals, while some very large clusters were only observed in the older animals. Figures 3F, L illustrate large ribbon clusters, which were only observed in 32-week-old animals. It is also noteworthy that panel F and the first image in lower panel D (Figure 3; asterisks) depict ribbons from 32-week-old mice without a nearby bassoon spot, which could indicate that these ribbons lack a membrane-anchor and thus likely represent floating ribbons.

The utricle is a remarkably dense tissue, with multiple layers of tightly-packed type I and type II VHCs. Especially for TEM sectioning, this poses an intrinsic problem, as distinction between striolar and extrastriolar VHCs can be immensely difficult, but may influence our results and interpretation. The 2D and 3D EM data obtained in this study did not provide a differentiation between the distinct zonal regions. Hence, we decided to perform a basic comparative analysis of ribbon parameters across aging type I VHCs from striolar and extrastriolar regions (Supplementary Figure S3). For this purpose, we bred *Ai14-Neurog1-creER^{T2}* knock-in mice (Koundakjian et al., 2007; Madisen et al., 2010; Druckenbrod and Goodrich, 2015) to sparsely express the red fluorescent protein tdTomato in a small subset of vestibular ganglion neurons. This strategy enabled us to trace individual neurons and clearly identify their afferent fibers with VHCs. By combining this with immunohistochemistry, we could then—apart from cellular location in the fixed utricle—either select individual VHCs with calretinin-positive and tdTomato-positive calyces (as indicative for calyx-only fibers in the striola) or calretinin-negative, but tdTomato-positive calyces (representative of the calyceal endings of dimorphic fibers in the extrastriolar region) and subject them to quantitative analysis. Using this approach in combination with confocal microscopy, we could establish the counts of ribbon spots and their volumes of individual type I VHCs that were randomly labeled in either the striolar or extrastriolar regions and extended this analysis for three cohorts covering a time period from P18 to 1.5 years of age. In line with previous work (Wan et al., 2019) and independent of location, we observed a decline in the overall ribbon spot counts (Supplementary Figures S3E, F). Yet, while we found a statistically significant increase in ribbon spot size with advancing age in the striolar region, such effects could not be detected in the extrastriolar region in these experiments (Supplementary Figures S3E', F').

While this approach offers interesting new insights, it also comes with a range of drawbacks: for example, one has to take into account that due to the limited lateral and axial resolution of confocal microscopy (the latter also applies to 2D-STED), small and dense ribbon clusters—as observed in our 2D TEM data—will appear as one large ribbon in immunofluorescence experiments. Therefore, the true ribbon number per VHC is likely to be underestimated. Even in our STED analysis, large appearing ribbons or clusters might still not be completely resolved as separated entities, and this way might escape correct quantification in confocal microscopy. Moreover, due to the very close spacing between floating ribbons and the AZ plasma membrane—predominantly below the diffraction limit of ~200 nm—parameters such as synaptic engagement could not reliably be investigated using this method.

Taken together, while all employed 2D techniques (i.e., random section TEM and STED microscopy) revealed a range of novel insights into VHC synaptic morphology and age-dependent structural alterations at VHC AZs, it became clear that—in addition to electron tomography and serial sectioning—a large-scale high-resolution 3D method is required to accurately determine the number of single ribbons and ribbon clusters per cell as well as ribbon membrane attachment and their true dimensions in 3D.

3D volume analysis of the basolateral compartment of VHCs reveals larger ribbons in mature type I VHCs

In order to investigate ribbon clusters in more contextual detail, we performed focused ion beam—scanning electron microscopy (FIB-SEM) to obtain 3D information of the entire basolateral compartment of individual VHCs. These data could then be used to assess various ultrastructural parameters, including presynaptic ribbons alongside individual SVs and the postsynaptic innervation—at lateral resolutions of 3 or 5 nm and an axial resolution of 5 nm. Thereby, morphological parameters including ribbon number, size and the location of ribbon clusters can be visualized (Figure 4). Since FIB-SEM is a very complex, expensive

10.3389/fcell.2023.1178992

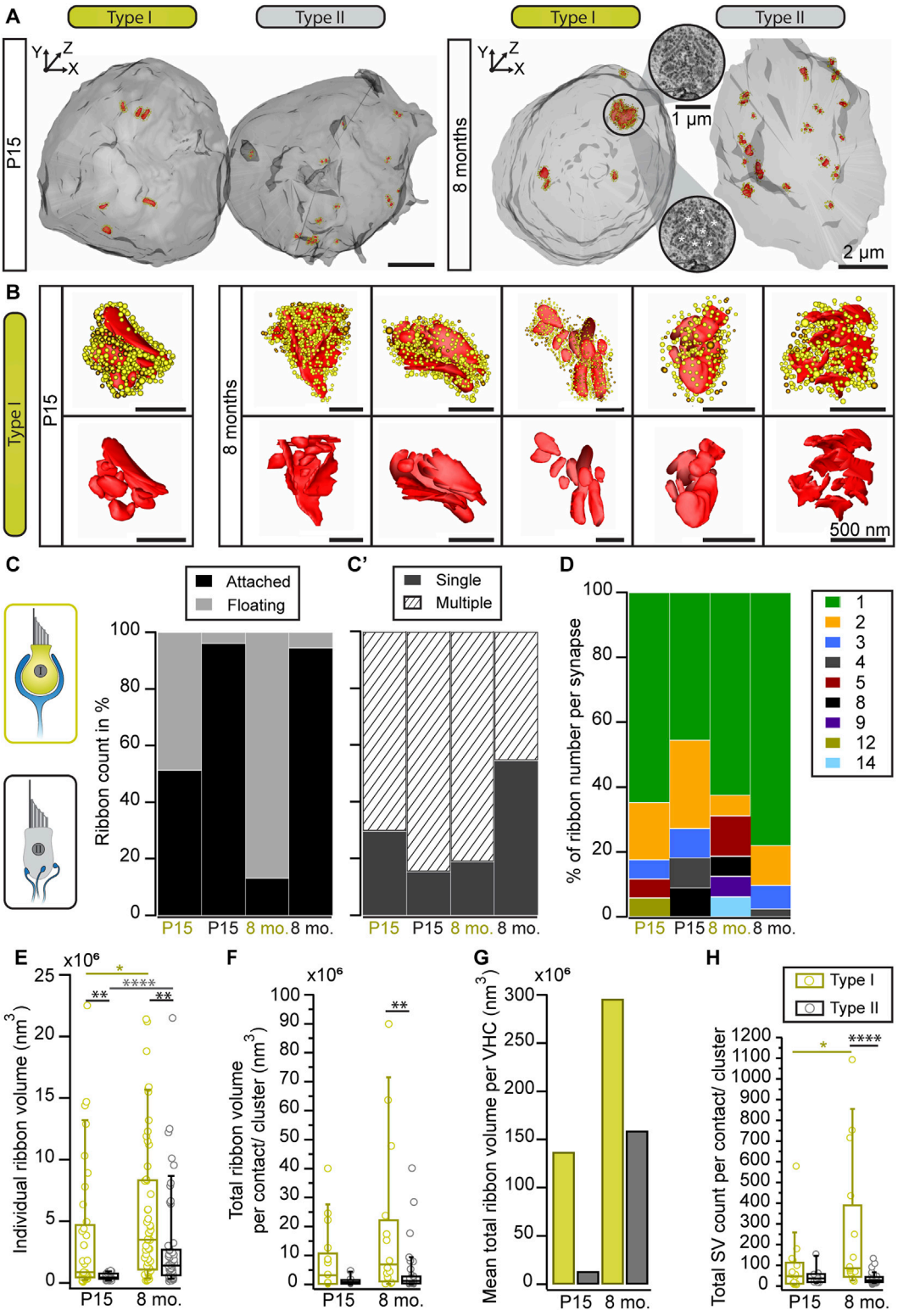

FIGURE 4
Ribbon cluster abundance in large volume data. **(A)** 3D models of type I and II VHCs from P15 and 8-month-old mice using FIB-SEM (top view). The P15 data set derived from type I VHCs with a complex calyx. The VHC bodies (light gray) contain numerous ribbon synapses (red) tethering SVs (yellow: ribbon-associated, orange: peripheral SVs). **(B)** Individual ribbon cluster segmentations of immature and mature type I VHCs. Upper row shows ribbon clusters with SVs, lower row displays the respective segmentation without SVs. **(C,C')** Bar graphs showing the distribution of attached vs. floating and single vs. multiple ribbons per VHC type and age group. **(D)** Analysis of the total ribbon count per synapse reveals more multiple ribbon numbers in type I VHCs. In type II VHCs, multiple ribbons per bouton could be observed in both age groups. **(E–G)** Ribbon size measurement data from both VHC types and age groups (Student's t-test or Mann-Whitney-Wilcoxon test). **(G)** Due to the limited number of total ribbon volumes per VHC, we refrained from performing a statistical analysis for this graph that displays the ratio between the categories young vs. old and type I vs. type II VHCs. **(H)** Boxplot illustrating

(*Continued*)

FIGURE 4 (Continued)
the SV numbers per synaptic contact or cluster (*p = 0.018, ****p < 0.0001 Mann-Whitney-Wilcoxon test). Note, the high SV count in type I VHCs with >1,000 SVs associated with a single ribbon cluster. For more detailed information see also Supplementary Table S6. P15 type I = 3 VHCs, N = 2 animals, n = 37 ribbons; P15 type II = 1 VHC, N = 1 animal, n = 26 ribbons; 8 mo type I = 4 VHCs, N = 2 animals, n = 53 ribbons; 8 mo type II = 2 VHCs, N = 2 animals, n = 55 ribbons.

and time-consuming method, we focused only on two representative ages: P15 for a maturing age group, and 8-month-old for an adult stage.

Consistent with the 2D random section analyses and electron tomography data, 3D segmentations from FIB-SEM volumes revealed the occurrence of ribbon clusters with increased frequencies in type I VHCs (Figures 4A, B; Movie 4 and 5)—particularly in mature animals. In fact, the clusters were larger than expected from the 2D TEM data or the immunohistochemistry and most ribbons within a cluster were indeed floating in the 8-months age group (Figure 4C; Supplementary Table S4). Conversely, type II VHCs exhibited predominantly attached ribbons in both age groups, which might be a result of a clear assignment—floating vs. attached—which is only possible in large 3D reconstructions (Figure 4C; Supplementary Table S4; Movie 6 and 7). Moreover, both VHC types showed higher numbers of–ribbon clusters in older ages (Figure 4C'). These ribbon clusters typically contain one to two (in type II VHCs) attached ribbons, which, in particular in old type I VHCs, are often surrounded by a number of floating ribbons. As mentioned above, in comparison to our 2D analysis, the ribbon counts per cluster were larger at both investigated ages (Figure 4C'; Supplementary Table S4; Movie 8)—with a maximum of 14 ribbons per cluster observed in a type I VHC (Figure 4D; Supplementary Table S4). While type II VHCs on average have more ribbon clusters per cell (P15 = 9 clusters, n = 1 VHC; 8 months = 5 clusters, n = 2 VHCs), fewer but more complex ribbon clusters are found in type I VHCs (P15 = 2 clusters, n = 3 VHCs; 8 months = 1.5 clusters per VHC; n = 4 VHCs). The average number of ribbons per cluster rose from P15 with 4.8–7.2 at 8 months in type I VHCs. In contrast, the average ribbon number per cluster remained constant in type II VHCs with advancing age (P15 = 2.4 ribbons, 8 months = 2.5 ribbons), largely consistent with our 2D data (Figure 2). In addition, there are on average fewer ribbons per cell observed in type I VHCs at both age groups (Supplementary Table S5) with fewer single membrane-attached ribbons (on average 2.5 ribbons) in 8-month-old type I VHCs compared to 8-month-old type II VHCs (on average 15 ribbons). For more detailed information about ribbon counts per individual VHC, the reader is referred to Supplementary Table S5, which provides absolute ribbon counts for the different ribbon categories.

Our analysis further revealed an age-dependent increase in individual ribbon volumes and a tendency towards more ribbon material regarding the total ribbon volume per VHC (Figures 4E–G; Supplementary Table S6). Collectively, the FIB-SEM data provide new insights into the differences between ribbon (cluster) dimensions in type I and II VHCs. While our 2D random section data suggested only a slight trend towards larger ribbons in type I VHCs (Figure 1I), the large volume data enabled more accurate quantification of individual ribbon volumes (Figures 4E–G; Supplementary Table S6) alongside the number of cluster-associated SVs. In fact, a single cluster could accumulate >1,000 SVs in our data sets (Figure 4H). Moreover, the summed ribbon volume per VHC indicated a trend towards an age-dependent increase in ribbon material in both VHC types, with type I VHCs containing more ribbon material than type II VHCs in both age groups (Figure 4G).

Movie 4 and 5: FIB-SEM visualizations of type I VHCs with 3D segmentation of single ribbons and ribbon clusters

Movies scanning through the representative FIB-SEM z-stacks of P15 (Movie 4) and 8-month-old (Movie 5) type I VHCs, showing 3D reconstruction of the VHC contours (transparent gray), part of the nuclei (dark gray), synaptic ribbons (red) and their corresponding SVs (yellow). Movie 4 displays two neighboring P15 type I VHCs likely from the striola that are enclosed by one complex calyx.

Movie 4 in Supplementary Presentation S1
Movie 5 in Supplementary Presentation S1

Movie 6 and 7: FIB-SEM visualizations of the basolateral compartment of type II VHCs with corresponding 3D segmentations

Movies scanning through the FIB-SEM z-stacks of P15 (Movie 6) and 8-month-old (Movie 7) type II VHCs. The corresponding 3D models depict VHC contours (transparent gray), part of the nuclei (dark gray), innervating nerve fibers (blue), mainly single attached ribbon synapses (red) and their corresponding SVs (yellow). Additionally, some afferent fibers possess multiple ribbons per bouton (Movie 6).

Movie 6 in Supplementary Presentation S1
Movie 7 in Supplementary Presentation S1

Movie 8: ribbon cluster formation of a type I VHC

Overview of a partial FIB-SEM z-stack showing a typical ribbon cluster formation at higher magnification of an 8-month-old type I VHC. Several floating ribbons can be observed in close proximity to the VHC membrane exhibiting no membrane attachment.

Movie 8 in Supplementary Presentation S1

Ribbon clusters may act as SV reservoirs

Our observation that ribbon clusters bind a large reservoir of SVs raised the question, if these SVs can actually still contribute to the SV cycle. The large number of SVs associated with the ribbon clusters—especially in type I VHCs—might either indicate (i) on-

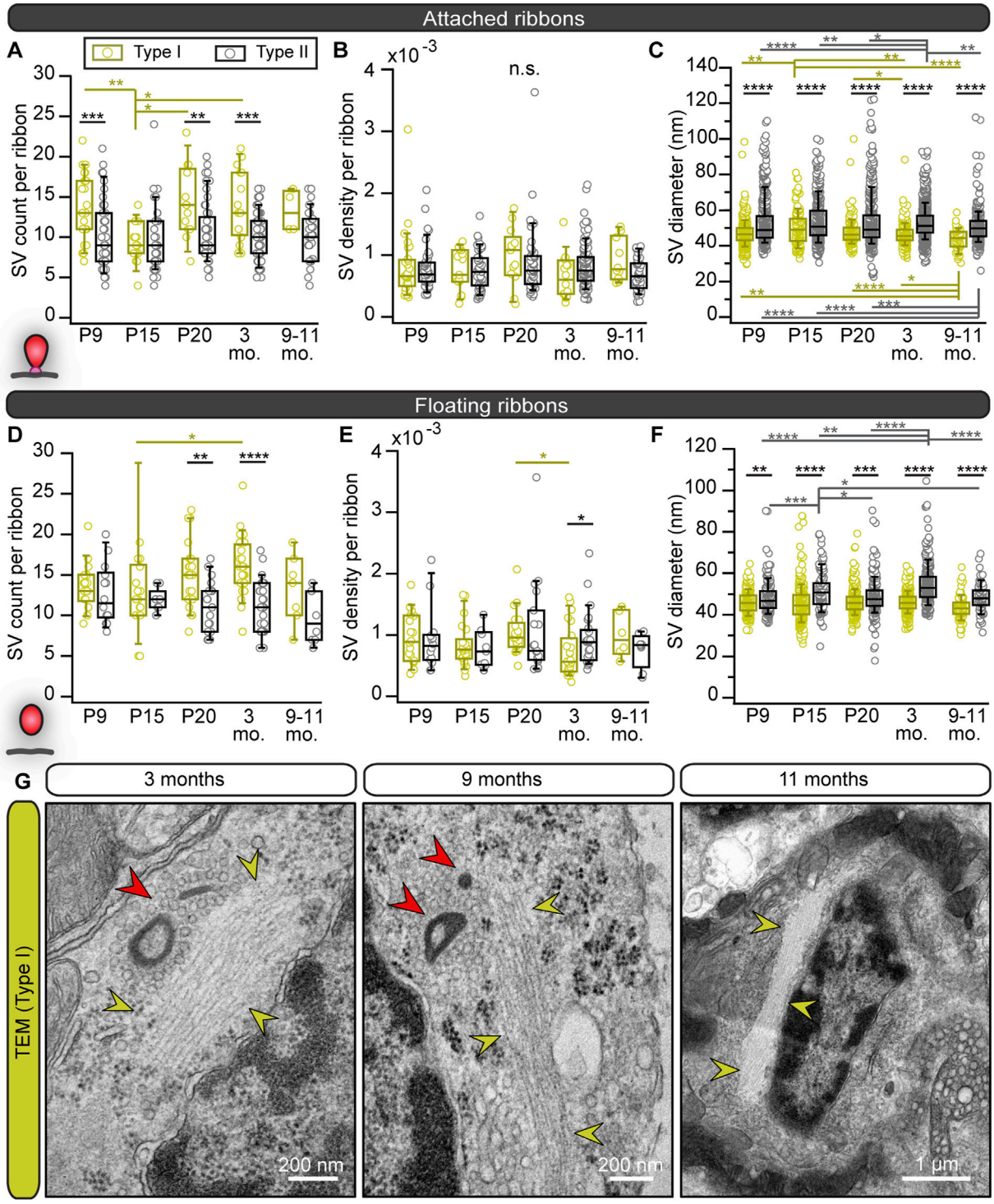

FIGURE 5
Smaller SV diameters but larger SV clouds around type I VHC ribbons close to filamentous structures. **(A–F)** Boxplots present the data for SV counts, their density and diameter measurements for attached and floating ribbons, respectively. **(G)** Electron micrographs from 2D TEM data display accumulations of filamentous cytoskeletal structures (yellow arrowheads) in type I VHCs of older ages, which were regularly detected nearby ribbon clusters (red arrowheads) with their corresponding excessive clouds of SVs. For more detailed information see Supplementary Tables S7, S8.

demand recruitable SV reservoirs or (ii) SV buffers that hold SVs that were removed from the release cycle (Figures 4B, H). To examine SVs in more detail, we first analyzed the total amount of SVs within 80 nm distance from the ribbons in our high resolution 2D TEM data set. For attached ribbons, we additionally distinguished between SVs in membrane proximity (MP-SVs: ≤25 nm distance from the AZ membrane and ≤80 nm from the presynaptic density) and ribbon-associated vesicles (RA-

SVs: first row of SVs around the ribbon within 80 nm) (Supplementary Figure S4), which represent two well-studied morphological SV pools at auditory and vestibular ribbon synapses and might give some indications about SV availability (Lenzi et al., 1999; Lenzi et al., 2002; Strenzke et al., 2016; Chakrabarti et al., 2018; Jean et al., 2018). Due to the missing attachment point of floating ribbons to the membrane, the ribbon orientation could not be identified and hence, only the total SV pool was analyzed for floating ribbons.

Results from floating and attached ribbons revealed a tendency towards higher numbers of total SV, MP- and RA-SV counts in type I VHCs especially at older ages, similar to the data from FIB-SEM (Figures 5A, D; Supplementary Figures S4A, B; Supplementary Table S7). However, the SV density of attached and floating ribbons, normalized to the ribbon surface area (Figures 5B, E), as well as the fraction of MP-SV and RA-SV pools revealed no age-related differences for both VHC types (Supplementary Figures S4C, D; Supplementary Table S7). Finally, SV diameters were measured since our previous study revealed a decrease in SV diameters upon development of IHC ribbon synapses (Michanski et al., 2019). Interestingly, SV diameters from attached and floating ribbons showed significantly larger SVs in type II VHCs compared to type I VHCs with no age-dependent effects (Figures 5C, F; Supplementary Table S8).

An extensive apico-basal microfilament network may stabilize aged type I VHCs

Lastly, from ~3 months on, type I VHCs exhibited prominent strands of longitudinal filaments that could represent cytoskeletal elements such as microtubules or actin filaments (Figure 5G). These strands were partially wrapped around the nucleus in a spiral manner, as segmented in our FIB-SEM data sets (Movie 9, Supplementary Figure S4F). About the function of these large cytoskeletal strands can only be speculated; however, similar structures—previously termed "microfilaments"—have been described in Heywood et al. (1975). If these microfilaments support ribbon (cluster) transport to the AZ remains elusive to date. Yet, in our previous study in cochlear IHCs, we described a potential involvement of microtubules in ribbon transport to the AZ due to close spatial proximity and co-localization of floating ribbon precursors with the microtubule-based motor protein KIF1a (Michanski et al., 2019). In addition, such microfilaments are likely also involved in maintaining cell shape and longitudinal stability.

Movie 9: filamentous network at the nucleus level can be traced in a partial FIB-SEM z-stack of an 8-month-old type I VHC

Movie displays a large microfilament network (highlighted with arrowheads) proximal to a ribbon cluster (highlighted by a red circle).

Movie 9 in Supplementary Presentation S1

Mature type I VHCs exhibit a set of larger mitochondria that reside closer to the AZ

Ribbons are designed for release sites with large membrane turnover and commonly operate in sensory systems characterized by tonic—probably high-rate—SV release. Continuous synaptic SV cycling upon tonic transmission might require high amounts of metabolic energy, i.e., ATP. Since production of ATP requires adequate mitochondrial function, we next assessed mitochondria abundance and morphology in our 3D FIB-SEM datasets. Indeed, in 8-month-old type I VHCs, the volume for a subset of mitochondria was enlarged as compared to the young controls with some mitochondria reaching sizes up to 100-fold larger than the average mitochondrion in the young type I VHC (volume of 4.29×10^7 nm^3; Figures 6A–E). However, the corresponding statistical analysis did not yield a significant difference. In contrast, much smaller size differences were detected within the cell of young and aged type II VHCs (Movie 10 and 11). The presence of some enlarged mitochondria in type I VHCs could further be observed with TEM starting at 3 months of age (Supplementary Figure S5).

Since mitochondria were suggested to importantly influence presynaptic activity through ATP, Ca^{2+} supply and buffering (Esterberg et al., 2016; Pickett et al., 2018; Wong et al., 2019), their number and distance to ribbons might change during maturation of synaptic machinery and structure. Indeed, our FIB-SEM data suggest a developmental rise of mitochondrial counts nearby synaptically-engaged ribbons in type I VHCs with a slight trend towards a closer proximity that was not observed in type II VHCs (Figures 6F, G). Here, the opposite was found with fewer mitochondria nearby ribbons in older animals.

Movie 10 and 11: 3D visualization of mitochondria from FIB-SEM z-stacks of P15 and 8-month-old type I and type II VHCs

Movies show 3D reconstructions of VHC contours (transparent gray), part of the nuclei (dark gray) and mitochondria (randomly colored).

Movie 10 (P15) in Supplementary Presentation S1
Movie 11 (8 months) in Supplementary Presentation S1

VHC ribbons show a high turnover

Since ribbon material seems to accumulate specifically in older type I VHCs, the question remains, where the observed floating ribbons originate from. Here, two scenarios can be envisioned: (i) at the end of their lifetime, 'old' ribbons detach (with SVs) for adequate degradation and resorption; however, this process might get corrupted with advancing age resulting in accumulation of ribbons close to the AZ, or (ii) new ribbons are constantly being formed in the cytosol and transported to the AZs; however, once there, the membrane-anchoring at the AZ might fail or become inefficient, thus leading to cluster formation. While given parts of

10.3389/fcell.2023.1178992

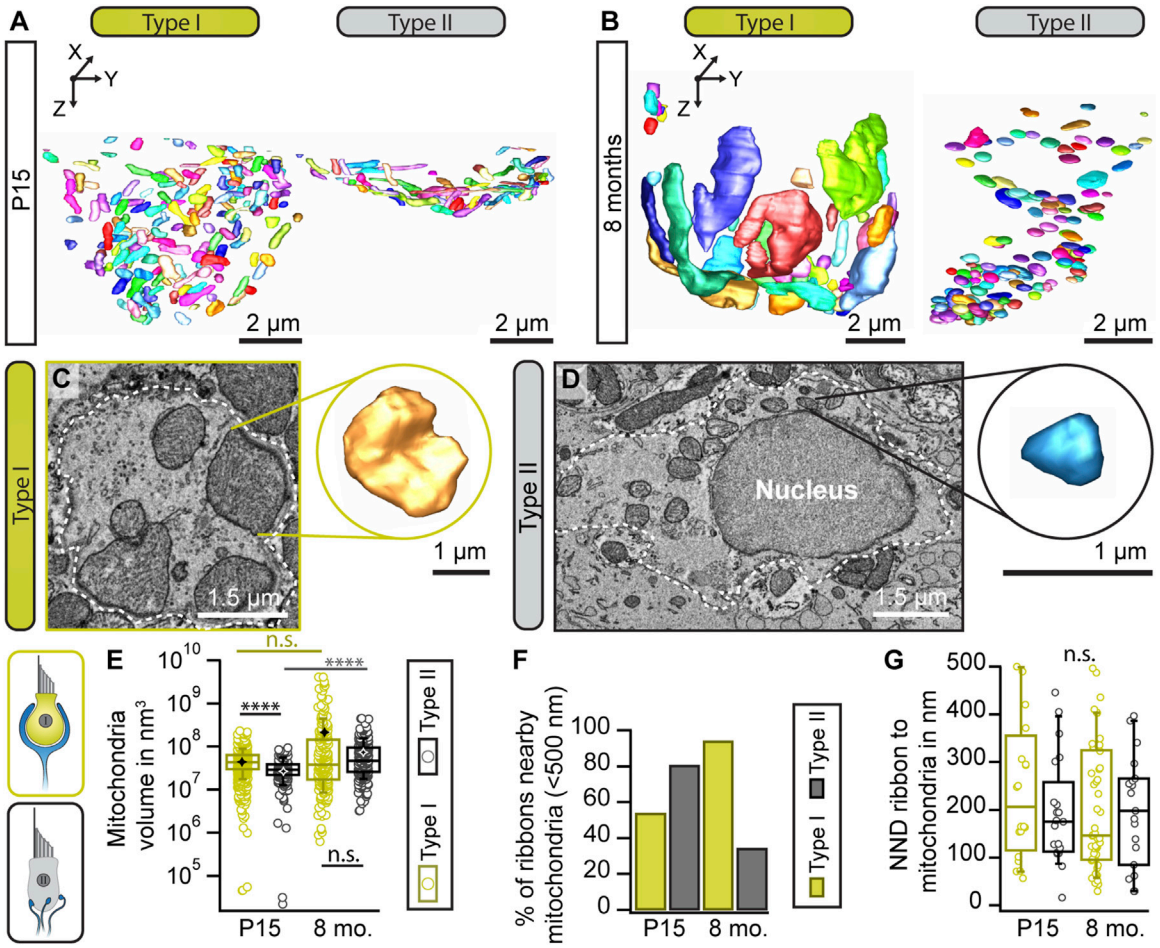

FIGURE 6
Enlargement of mitochondrial volume with advancing age. **(A,B)** Representative 3D segmentations of mitochondria in type I and II VHCs at indicated ages. **(C,D)** Single sections from the large FIB-SEM datasets illustrating the mitochondrial size difference between type I and type II VHCs. Insets illustrate 3D reconstruction of the individual mitochondrion. **(E)** Analysis of the mean mitochondrial volumes (indicated by black and white stars) presents a consistent trend of larger mitochondria in mature animals. However, no statistically significant difference was detected for type I VHCs when comparing the related data for both age groups. **(F)** Percentage of mitochondria within <500 nm of the closest ribbon in both age groups and VHC types. **(G)** Nearest neighbor distance (NND) of mitochondria-proximal ribbons (located <500 nm to the closest mitochondrion), *n. s.* $p > 0.05$ (*t*-test). P15 type I = 3 VHCs, N = 2 animals; P15 type II = 1 VHC, N = 1 animal; 8 mo type I = 4 VHCs, N = 2 animals; 8 mo type II = 2 VHCs, N = 2 animals.

our current data may support either scenario, we next set out to clarify this issue directly via metabolic labeling.

For this purpose, we made use of nanoscale secondary ion mass spectrometry (NanoSIMS). In NanoSIMS, a primary Cs^+ beam irradiates the sample and causes the sputtering of secondary particles from the sample surface. These particles are partly ionized and subsequently identified by mass spectrometry. In these experiments, mice were fed for 14 or 21 days with a modified diet, in which every new nitrogen atom is provided as the heavy ^{15}N stable isotope variant that, in concentrations higher than ~0.4% can be unambiguously distinguished from the far more abundant (>99%) naturally-occurring ^{14}N. This approach provides unbiased insights into the composition of the large majority of cellular structures, since not only proteins, but also nucleic acids, lipids (e.g., phospholipids as phosphatidyl-choline, -ethanol amine or–serine, and sphingolipids) and sugars (e.g., N-acetylated glycans) contain nitrogen atoms. Hence, it serves as an excellent approach to identify "old" vs. "new" material in VHCs by calculating the $^{15}N/^{14}N$ ratio. Typically, this approach allows for lateral resolutions ~50–100 nm and axial resolutions of ~5–10 nm. To now relate turnover rate to cellular ultrastructure, we combined NanoSIMS with 110 nm ultrathin sections of conventionally-embedded samples (Figure 7).

Surprisingly, we found that both the attached and floating ribbons contained high levels of ^{15}N. In fact, the majority of the ribbons showed a higher turnover than all other cellular components we analyzed (e.g., cytosol, nuclei or mitochondria; Figure 7C; Supplementary Table S9). Several aged ribbons could be found exclusively in the membrane-attached population when investigating animals fed with the isotopic diet for 14 days; however, such ribbons were no longer

10.3389/fcell.2023.1178992

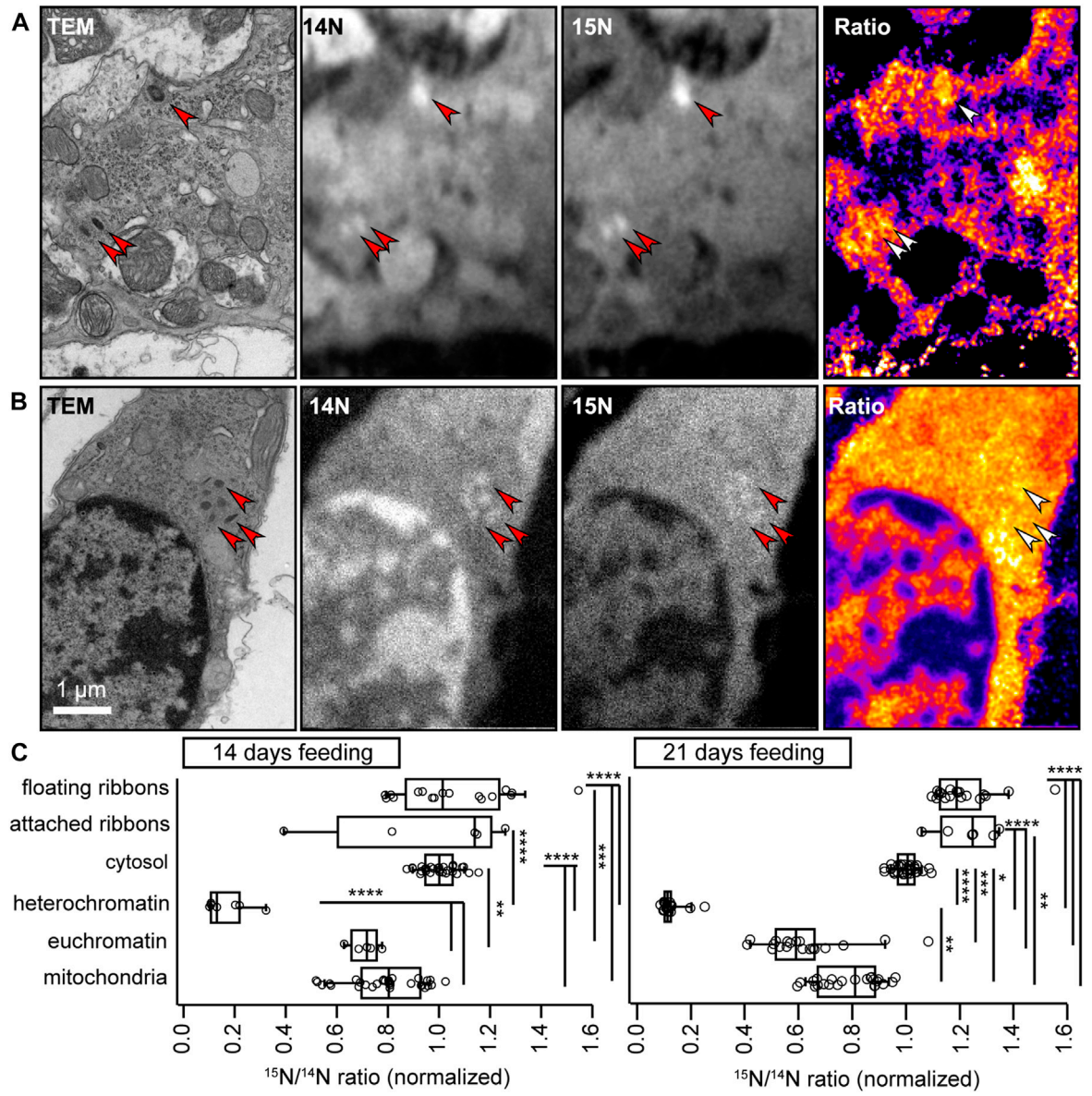

FIGURE 7
NanoSIMS analysis of VHC ribbons. **(A,B)** To measure protein turnover in VHCs, newly synthesized cellular components were labeled with ^{15}N via a modified diet. 10–14 months old wild-type mice were subjected to this diet for 14 days, before dissecting the VHCs and imaging them first in TEM and then in NanoSIMS. The arrowheads point to several ribbons, with **(A)** indicating a type II VHC and **(B)** a type I VHC. In **(A)** the topmost ribbon is membrane-attached, while the other two are floating. In **(B)**, all six ribbons are floating in the cytosol. The ^{14}N and ^{15}N images indicate that the protein-dense ribbons are easily visualized in NanoSIMS, as bright (nitrogen-intense) spots. The ratio images show the ^{15}N (newly synthesized) signal divided by the ^{14}N (old) signal. The ribbons in **(A)** are considerably richer in ^{15}N than the ones in **(B)**. **(C)** The analysis for organs from animals fed with ^{15}N for 14 days indicates the $^{15}N/^{14}N$ ratios for 13 attached ribbon and 40 floating ribbon measurements, from 15 series of NanoSIMS measurements, from 4 organs. The floating ribbons are substantially more enriched in ^{15}N than mitochondria or heterochromatin ($p < 0.0001$, ANOVA test followed by *post hoc* Tukey test). The attached ribbons are also significantly more enriched in ^{15}N than heterochromatin ($p < 0.0001$, ANOVA test followed by *post hoc* Tukey test). A similar analysis for organs from animals fed with ^{15}N for 21 days shows that the ribbons are now substantially richer in ^{15}N than all other cellular components ($p < 0.0001$, KW test with multiple comparison correction; 6 to 25 measurements). The attached ribbons low in ^{15}N (old) have now disappeared, suggesting that ribbons are replaced on a 1–3-week timeline. $N_{14\ days} = 2$ animals; $N_{21\ days} = 2$ animals.

identifiable after 21 days of feeding. Thus, our data suggest that: (i) VHC ribbons exhibit considerable turnover dynamics exceeding the ones observed for other organelles, (ii) different ribbons show different levels of turnover, even in the same cell—with a full exchange taking place every 1–3 weeks and importantly (iii) that floating ribbon clusters might be exclusively composed of newly formed ribbons, therefore pointing to normal formation and transport, but a faulty AZ membrane-attachment mechanism with advancing age.

10.3389/fcell.2023.1178992

Discussion

The present study describes several morphological alterations in aging utricular VHCs (Figure 8). Specifically, we found that: (i) both, VHC ribbons and mitochondria (mainly in type I VHCs), undergo drastic changes in shape and increase in size/volume during the aging process. (ii) Ribbons, successively, are found detached from the AZs and these floating ribbons start to accumulate, particularly in type I VHCs, in an age-dependent manner, thereby causing a remarkable increase in the total amount of ribbon material per cell. (iii) These floating ribbons are decorated with full sets of seemingly mature SVs and form clusters within the cytoplasm, often in proximity to the AZ. (iv) Ribbons within these clusters are mainly composed of newly-synthesized proteins. Finally, (v) our data suggest that these 'new' ribbons might collectively fail at the final membrane-anchoring step, potentially due to an age-dependent AZ depletion of the ribbon-anchoring protein bassoon.

VHC ribbon synapses undergo structural alterations in an age-and cell-type-dependent manner

First and foremost, this study reveals striking differences in the ribbons decorating type I and type II VHCs, and even more so when compared to the ribbons in closely-related cochlear IHCs. For example, our most prominent finding is a progressive accumulation of "floating", i.e., not membrane-attached ribbons that, instead of being degraded, form large clusters in type I VHCs. While previous studies already reported on the occurrence of such cytosolic ribbon aggregates—for example, in VHCs of the murine *crista ampullaris*, ribbon clusters could be observed as early as P2-4 (Nordemar, 1983), our study provides the first detailed longitudinal analysis of this phenomenon ranging from immature to late adult states.

Our observations in the maturing and older VHCs, approximately 1 year of age, stand in stark contrast to the developmental maturation of auditory IHCs, in which floating ribbons seem to present a characteristic, but transient, feature of cellular immaturity that disappears prior to hearing onset (Sobkowicz et al., 1986; Wong et al., 2014; Michanski et al., 2019). Consistent with our findings, floating ribbons were previously observed solely in adult type I VHCs, here specifically in female C57BL/6N mice; however, overall still more single ribbons than ribbon clusters were described (Park et al., 1987; Woods and Park, 1987). We assume that the ribbon number per cell and the ribbon number per cluster might have been underestimated due to the limitation of 2D data sets. Several previous studies performing random or serial sectioning for TEM in different species and ages reported different predominant ribbon morphologies in the VHCs. While some investigations state that type I VHC ribbons predominantly exhibit a single, small and spherical appearance (Yamashita and Ohmori, 1991; Lysakowski, 1996; Lysakowski and Goldberg, 1997; Lysakowski and Goldberg, 2008), other researchers observed more variable appearances such as elongated and multiple ribbons in type I VHCs (Engström et al., 1972; Park et al., 1987; Woods and Park, 1987; Sans and Scarfone, 1996). Most of the studies lack a quantification regarding the ratio of membrane attached and floating ribbons, however, Sans and Scarfone (1996) already characterized floating ribbons in human type I cells. This observation is in line with numerous TEM images that depict multiple ribbons forming a cluster within the cytosol and exhibiting a substantial distance to the cell membrane (Engström et al., 1972; Nordemar, 1983; Favre et al., 1986; Park et al., 1987; Woods and Park, 1987; Sans and Scarfone, 1996; Lysakowski and Goldberg, 2008). Since membrane-attachment in a previous or subsequent section cannot be excluded in such cases, the interpretation of such 2D TEM analyses remains limited. Interestingly, using confocal microscopy, Sadeghi et al. (2014) observed partially misaligned presynaptic and postsynaptic components in rat type I VHCs. However, this study did not include a membrane marker, thus, conclusions regarding the attachment of ribbons to the membrane cannot be done. We were now able to observe ribbons and their association with the plasma membrane in unprecedented detail using state-of-the-art 3D techniques, such as electron tomography and FIB-SEM. Here, FIB-SEM in particular allowed for a comprehensive analysis of all AZs within a given VHC, not just a limited selection and/or single AZs. Thus, the majority of estimates in our study are based on the 3D volume reconstructions, which provide more accurate numbers of single ribbons as well as floating ribbons and ribbons within clusters. At the age of 8 months, we found an average of approximately 2.5 single (membrane-attached and floating) ribbons and

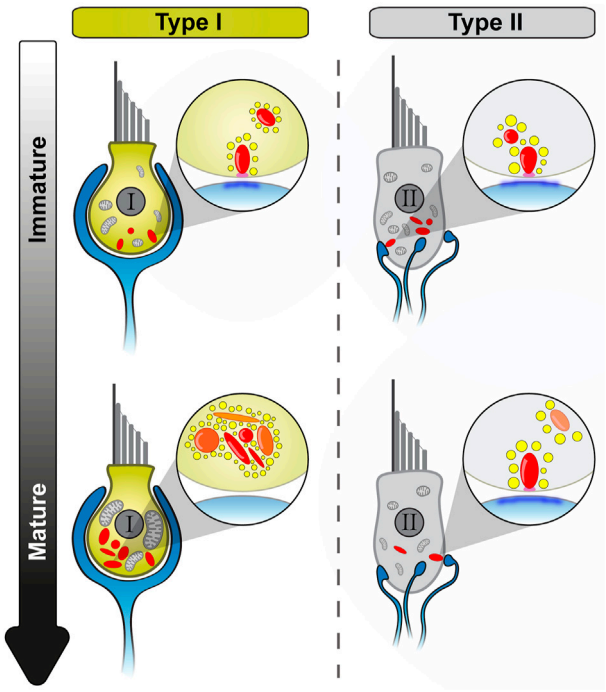

FIGURE 8
Schematic overview of utricular VHC ribbon synapse maturation and with advancing age. Summary of the main morphological observations during utricle development. While type II VHCs show very similar developmental events as detected in cochlear IHCs, type I VHCs undergo a distinct maturation process. Light blue: afferent contacts, red: synaptic ribbons (young/newly formed ribbons: transparent, old ribbons: opaque), yellow: SVs, magenta: presynaptic density, dark blue: PSD, light gray: mitochondria.

~11 ribbons within clusters in type I VHCs. In type II VHCs at the same age on average 15 ribbons were single (floating and attached at the plasma membrane) and 12.5 organized in clusters. The latter were smaller, containing a maximum of 4 ribbons, whereas up to 14 ribbons were found in a single cluster in type I VHCs. Interestingly, ribbon accumulations and floating ribbons were also detected in type I VHCs from a human fetus (Favre et al., 1986; Sans and Scarfone, 1996), indicating a similar arrangement in humans.

Morphological similarities and differences between type I and type II VHC ribbons

While ribbons in both VHC types are of various sizes and shapes, an age-dependent transformation towards elongated ribbons was observed in type I VHCs only. In contrast, ribbon shape distributions in type II VHCs remained much more uniform across ages. Both cell types mostly anchor one to two ribbons per AZ and in both, the number of membrane-attached ribbons per AZ peaks at P15, with a small proportion of AZs involving three or four membrane-attached ribbons, in type II and I VHCs, respectively. Our results in type II VHCs are in line with a previous study in the vestibular end organs of adult guinea pigs showing that the AZs of type II VHCs mainly harbor single synaptic ribbons, while ~20% of afferent terminals are opposed by two or more ribbons (Sjöbäck and Gulley, 1979).

A morphological characteristic that seems to be conserved between distinct hair cell types is the presence of translucent core ribbons (Engström et al., 1972; Favre and Sans, 1979; Sjöbäck and Gulley, 1979; Liberman, 1980; Sobkowicz et al., 1982; Park et al., 1987; Woods and Park, 1987; Lysakowski, 1996; Lysakowski and Goldberg, 1997; Stamataki et al., 2006; Lysakowski and Goldberg, 2008; Michanski et al., 2019). While the previous studies suggested that these "fenestrated" ribbons represent the final stages in the lifespan of a ribbon, we could not find any age-related differences in their occurrence. This is in line with the work of Park et al., (1987), Woods and Park (1987) who observed such ribbons in both VHC types in the saccule of young and old mice, however, without the knowledge of the actual "ribbon age". Since translucent cores tend to occur in larger ribbons, we hypothesize that such morphological changes may appear due to RIBEYE packaging limitation. Future studies employing NanoSIMS analysis might clarify whether the age of ribbons is a defining factor in the occurrence of this phenomenon.

Microfilaments may serve as a means of transport for VHC ribbons

Ribbons were shown to form in the cytoplasm via auto-aggregation of the main structural scaffold protein RIBEYE (Magupalli et al., 2008). These aggregates form SV-tethering ribbon precursors that are then transported to the AZ in a microtubule (MT) and kinesin-dependent process (Michanski et al., 2019). However, VHCs are dominated by the occurrence of large strands of dense microfilaments that align with the apico-basal axis of mature type I VHCs. These filaments were previously described in otocyst VHCs during early development and were interpreted to be involved in nucleus migration (Heywood et al., 1975). While the molecular nature of these microfilaments remains elusive, functionally they might be involved in transport of sub-cellular structures, as they occupy a large apico-basal volume in aged type I VHCs. Moreover, since microfilament bundles were often observed in close proximity to ribbon clusters, it is conceivable that they contribute to ribbon transport towards the AZs. Alternatively, they might solely provide structural stability to VHCs. We would additionally like to point out that these filamentous structures sometimes also resemble smooth endoplasmic reticulum. However, since we also observe these structures in cross sections, where they appear as bundles of filamentous structures rather than membranes, this strongly suggests that they are indeed of cytoskeletal nature. Future studies will be required to establish the molecular identity and function of these microfilaments.

Aging affects mitochondrial volumes of utricular type I VHCs

The production, transport, and maintenance of ribbons, together with continuous tonic synaptic transmission are energy-demanding processes. Age-dependent cellular alterations, which ultimately attenuate release efficiency, may lead to energetic imbalance at the synapse that needs to be compensated. Such a scenario may be supported by our findings of enlarged synaptic mitochondria observed in aging type I VHCs. Mitochondria power the cells by producing ATP (Harris et al., 2012), which is for example required to synthesize glutamate (Waagepetersen et al., 2003), fill SVs with neurotransmitter molecules, prime SVs for release at the AZ membrane (Forgac, 2007; Verhage and Sørensen, 2008; Yao and Bajjalieh, 2008) or fuel local translation (Rossoll and Bassell, 2019). Moreover, an increased production of mitochondrial ATP is required for exocytosis and the endocytosis-based recycling of SVs, which even causes depletion of ATP during heavy cycling (Rangaraju et al., 2014). Therefore, it is not surprising that mitochondria were described to play a key role in quantal synaptic transmission (Smith et al., 2016; Wong et al., 2019). In the present study, we found that a fraction of mitochondria were drastically enlarged in older type I VHCs, which corroborates previous findings of generally larger diameters in type I VHCs employing TEM (Goldberg et al., 1992; Eatock et al., 1998; Rüsch et al., 1998) and of extremely large volumes of a subset of mitochondria from the subcuticular region of type I VHCs in adult chinchilla utilizing electron tomography (Vranceanu et al., 2012). In contrast, the latter study did not report enlarged mitochondria in other type I cell regions. Additional serial section TEM investigations conducted on young and adult animals from diverse species did not observe substantial size differences between type I and II VHCs (Engström et al., 1972; Woods and Park, 1987; Goldberg et al., 1990; Yamashita and Ohmori, 1991; Lysakowski, 1996; Lysakowski and Goldberg, 1997; Lysakowski and Goldberg, 2008). However, these previous studies lacked a comprehensive size/volume quantification or morphology description of mitochondria. We addressed the 2D limitation by utilizing advanced large volume

FIB-SEM, which enabled us to achieve a detailed analysis of mitochondria sizes in 3D. A similar observation of an performance- and age-dependent mitochondrial volume increase was reported e.g., in the hippocampus (Pathak et al., 2015; Smith et al., 2016; Cserép et al., 2018) and calyx of Held (Thomas et al., 2019), where mitochondria were found to be larger after hearing onset. The size enlargement was interpreted to support higher firing rates in auditory information processing to meet the higher energy demands and, thus, was proposed to be functionally-coupled to the release mode (Thomas et al., 2019). On one hand, since fewer ribbon synapses are attached in older type I VHCs, these ribbons have to work harder to achieve the same task, which might require higher energy. On the other hand, the accumulation of relatively young synaptic ribbons, together with a large number of SVs, also indicates an increased local translation of ribbon material, another energy demanding process (Rossoll and Bassell, 2019). Finally, the mitochondria ultimately supply energy for maintaining ionic homeostasis during continuous depolarization and hyperpolarization of the hair cells, which may be essential for type I VHCs since the supporting cells have no (or limited) access to the synaptic cleft.

Notably, in several studies, both vestibular and auditory disorders were associated with mitochondrial dysfunction (Fischel-Ghodsian et al., 2004; Kokotas et al., 2007; Iwasaki et al., 2011; Böttger and Schacht, 2013; Requena et al., 2014), which might also cause enlarged mitochondria.

The formation of ribbon clusters increases with age and is a striking hallmark of older type I VHCs

With increasing age, the proportion of membrane-attached ribbons steadily declines, however, the prominence of large ribbon clusters, particularly in type I VHCs, successively increases. Here, accumulations of more than ten ribbons could be shown to incapacitate several hundreds of SVs within a single cluster. While clusters can also be found in type II VHCs, their size typically remains moderate, commonly not exceeding two to four ribbons.

In our study, both types of VHCs have floating ribbons throughout adulthood, but with different abundance. The proportion of floating ribbons in type II VHCs remains mostly constant throughout the investigated ages (starting from early second postnatal week) and decreases modestly by ~1 year of age, but detached ribbons never fully disappear. It is important to note that in rodents new type II VHCs can be formed throughout adulthood, although the regenerating potential is moderate (Forge et al., 1993; Forge et al., 1998; Kawamoto et al., 2009; Lin et al., 2011; Golub et al., 2012; Slowik and Bermingham-McDonogh, 2013; Burns and Stone, 2017; Hicks et al., 2020). Therefore, we cannot completely rule out the possibility that type II VHCs containing floating ribbons in old animals may represent (at least in part) freshly-regenerated and hence immature hair cells. Future experiments will be required to clarify this issue. Such a scenario is unlikely to take place in type I VHCs. In these cells, floating ribbons represent the vast majority of the total ribbon population in older mice, which additionally argues against these ribbons being a signature of newly regenerated cells. A hallmark of type I VHCs is their use of two modes of synaptic transmission, a classical quantal and a nonconventional non-quantal mode of synaptic transmission (reviewed in (Eatock, 2018; Mukhopadhyay and Pangrsic, 2022)). To what degree one or the other mode of transmission may operate in individual cells, and possibly influence and support each other to enable transmission of vestibular information, remains under investigation (Songer and Eatock, 2013; Highstein et al., 2015; Contini et al., 2020; Spaiardi et al., 2022). One could speculate that floating ribbons may be a signature of "low" demand for quantal synaptic transmission. If so, the questions to address in the future would be, whether their abundance in cells changes dynamically upon demand or varies in distinct cell subpopulations? While, due to different technical limitations, we could not assess the absolute numbers of floating and attached ribbons in a large number of individual VHCs, we so far found no indication of distinct subpopulations of type I VHCs with different abundance of floating vs. attached ribbons, which remains an interesting question to be revisited in the future.

An age-dependent deficit in ribbon membrane-anchoring at the AZ might give rise to floating ribbon clusters

The high abundance of floating ribbons in adult VHCs is highly unusual for ribbon-type synapses; however, various scenarios can be envisioned that may explain this phenomenon: (i) in the process of synaptic degeneration, ribbons may detach from the AZ membrane prior to degradation and/or recycling, thus accumulating in the cytoplasm, (ii) the process of formation and attachment of ribbons may be activity-dependent and highly dynamic, with cytosolic clusters in AZ proximity serving as a 'reserve pool' of ribbons that may be recruited to, or retracted from, the plasma membrane upon a change in demand—thus rapidly adding or removing substantial amounts of release-ready SVs—or (iii) 'new' ribbons may be formed continuously, but with increasing age, lose the ability to attach adequately at the plasma membrane.

The first hypothesis may be supported by a recent study that reported a selective loss of synaptic ribbons in extrastriolar type I VHCs of old mice (Wan et al., 2019). This may possibly be associated with detachment and subsequent degradation of synaptic ribbons, but such a mechanism remains to be unambiguously demonstrated.

Regarding the second hypothesis, floating ribbons were found in albino rats that were brought to space (Ross, 1994; Ross, 2000), suggesting a loss of attached ribbons due to a reduction of synaptic activity in response to hypogravity. However, since floating ribbons as well as ribbon clusters in rodents and humans are also present under normal-gravitational conditions, this explanation appears rather unlikely. Moreover, a significant decline of evoked vestibular potentials could only be detected at an age of 2 years in mice (Wan et al., 2019). Alternatively, floating ribbons may act as a dynamic reserve pool to supplement existing (or replace end-of-lifetime)

ribbons as well as SVs in case of changes in demand. In this context, our NanoSIMS data revealed that some ribbons within a given cluster were slightly older than others and ribbons were newly formed and possibly partially replaced within a time line of 1–3 weeks. However, ribbons were considerably younger compared to other subcellular structures such as mitochondria. The extent of structural plasticity of ribbons is only partly understood to date; yet, in other sensory systems, such as retinal photoreceptors or pinealocytes, ribbons were shown to adapt their shape in response to the cellular state of activity (Vollrath and Seidel, 1989; Spiwoks-Becker et al., 2004; Fuchs et al., 2013; Voorn and Vogl, 2020). Of particular interest here is the observation that photoreceptor ribbons apparently regulate their size by pinching off or fusing with SV-bearing precursor spheres upon changes in illumination (Spiwoks-Becker et al., 2004). As discussed above, the abundance of VHC ribbon synapses may change in hypogravity (Ross, 2000; Sultemeier et al., 2017). If floating ribbons in VHCs also act as a reserve pool for SVs, is questionable. Judging from the low amount of depolarization-evoked membrane capacitance change (reporting SV fusion with the plasma membrane) in young type I cells (Vincent et al., 2014; Spaiardi et al., 2022), it appears unlikely that hundreds of SVs were in place to support very high rates of exocytosis and replenishment.

Finally—and in our opinion most likely—the occurrence of ribbon clusters may be a result of an age-dependent degenerative processes that affect stable ribbon anchoring at the AZ membrane. Our NanoSIMS data revealed that floating ribbons in particular have a high protein turnover, thereby arguing in favor of the idea that these ribbons represent the accumulation of 'new' ribbons. In support of this hypothesis, our FIB-SEM data further indicate that throughout the VHC lifespan additional ribbon material is formed and the total amount steadily increases. Either, the protein synthesis of ribbon material is not controlled well enough anymore or, in combination with the apparent reduction of bassoon levels at the AZ, render a scenario most likely in which ribbon synthesis and transport remain intact, but anchoring at the release site fails. Since bassoon is a well-characterized scaffold essential for adequate ribbon attachment to the AZ membrane across different sensory systems (Dick et al., 2003; Khimich et al., 2005), its involvement in this process would be expected. While the exact molecular mechanisms remain to be determined, our work adds important novel insights into VHC ribbon synapse physiology and thus provides new directions for future studies.

Materials and methods

Animals

C57BL/6J, CBA/J and C57BL/6JRj (Janvier laboratory) wild-type mice of either sex between the postnatal day (P)9 and 11 months were deeply anesthetized with CO_2 and sacrificed by decapitation or cervical dislocation for immediate dissection of the utricle. For a subset of experiments, a Cre-dependent tdTomato reporter strain (*Ai14*; #007908 Jackson Laboratory; (Madisen et al., 2010); was crossbred with a *Neurog1*^{CreERT2} mouse line (#008529 Jackson Laboratory; (Koundakjian et al., 2007); to sparsely label random vestibular ganglion neurons. All experiments complied with national animal care guidelines and were approved by the University of Göttingen Board for Animal Welfare and the Animal Welfare Office of the State of Lower Saxony.

Immunohistochemistry, confocal and super-resolution STED microscopy

The inner ears were extracted from C57BL/6J mice at the age of 2 and 32 weeks. Small aperture was created in the bone just above the utricle with forceps. The pigmented membrane was carefully cut open to expose the utricle underneath. The entire inner ear was then transferred to 4% formaldehyde in phosphate buffer saline (PBS: Sigma #P4417, Germany) on ice for about 45 min to allow fixation of the tissues. Next, the sample was washed in deionized water for up to 1 min and then briefly (ca. 30 s) transferred to TBD-1 (Shandon TBD-1™ Rapid Decalcifier, Ref# 6764001) for decalcification, which was followed by another brief wash in deionized water at room temperature. The fixed and decalcified utricle was then carefully extracted from the inner ear using fine forceps and transferred to PBS.

The utricles were washed 3 times in PBS for 10 min each, followed by blocking with Goat Serum Dilution Buffer (GSDB: 16% normal goat serum, 450 mM NaCl, 0.3% Triton X-100, and 20 mM phosphate buffer, at pH 7.4) for 1 h at room temperature in a wet chamber. The organs were then incubated overnight in a primary antibody concoction prepared in GSDB at 4-8°C in a wet chamber. The following day the organs were washed 3 times in wash buffer for 10 min each and then incubated in a secondary antibody dilution in GSDB for 1 h in a light protected wet chamber at room temperature. Finally, they were washed again 3 times in wash buffer before being mounted on microscopy slides with mounting medium containing Mowiol 4–88 and DABCO (Carl Roth, Germany) or ProLong Glass antifade mounting medium (ThermoFisher, Germany). The following antibodies and dilutions were used: chicken-anti-calretinin (Synaptic Systems, Germany, dilution 1:200), rabbit-anti-piccolino (Synaptic Systems, Germany, dilution 1:200), rabbit-anti-RIBEYE (Synaptic Systems, Germany, dilution 1: 200), mouse-anti-bassoon (Abcam, Germany, dilution 1:300), mouse-anti-CtBP2 (BD Biosciences, United States, dilution 1: 200) and rabbit anti-dsRed (Clontech, dilution 1:200) as well as a directly Atto-565 conjugated anti-RFP nanobody (NanoTag, dilution 1:100). The secondary antibodies used were: Alexafluor488-labeled goat-anti-chicken (ThermoFisher Scientific, United States, dilution 1:200), Alexafluor594 labeled goat-anti-mouse (ThermoFisher Scientific, United States, dilution 1:200) or STAR635p-labeled cameloid anti-mouse IgG1 nanobodies (NanoTag, dilution 1:100), as well as STAR580-labeled cameloid anti-rabbit nanobodies (NanoTag, dilution 1:100) or STAR635p-labeled goat-anti-rabbit (Abberior, Germany, dilution 1:200). Confocal and high resolution 2D-STED images were acquired using an Abberior Instruments Expert Line STED microscope equipped with 488, 561 and 640 nm excitation lasers, STED laser at 775 nm (1.2 W), and a ×100 oil immersion objective (1.4 NA, Olympus). Images

were acquired using the same microscope settings, analysed and processed in Fiji/ImageJ software (Schindelin et al., 2012) or Bitplane Imaris 9.6.1 (Oxford Instruments), and assembled in Affinity Designer 1.10.5 for display.

Conventional embedding and transmission electron microscopy

Utricle organs from mice ranging in age between P9 to 11 months were isolated in HEPES Hank´s solution, which contained (in mM): 5.36 KCl (746436, Sigma, Germany), 141.7 NaCl (746398, Sigma, Germany), 10 HEPES (H3375, 006K5424, Sigma, Germany), 0.5 $MgSO_4$-$7H_2O$ (Sigma, Germany), 1 $MgCl_2$ (M2670, Sigma, Germany), 2 mg/mL D-glucose (G8270-1 KG, Sigma, Germany), and 0.5 mg/ml L-glutamine (G3126-100G, #SLBS8600, Sigma, Germany) and was adjusted to pH 7.2, ~300 mmol/kg. First the inner ear was dissected and the vestibular bone tissue was carefully removed. The inner ear was afterwards placed into a petri dish filled with proteinase XXIV solution (P 8038-100 MG, Th. Geyer, Germany; 50 mg/mL in HEPES-HANKS solution, w/v) for 5 min at room temperature to facilitate the removal of the otolithic membrane overlying hair bundles of the utricle. In fresh HEPES Hank's solution, the otolithic membrane was then removed and the exposed utricle was excised.

Conventional embeddings of vestibular organs were performed according to our previous studies (Wong et al., 2014; Strenzke et al., 2016; Michanski et al., 2019). In brief, the organs were fixed immediately after dissection with 4% paraformaldehyde (0335.1, Carl Roth, Germany) and 0.5% glutaraldehyde (G7651, Sigma, Germany) in PBS (P4417, Sigma, Germany; pH 7.4) for 1 h on ice followed by a second fixation step overnight with 2% glutaraldehyde in 0.1 M sodium cacodylate buffer (v/v, pH 7.2) at 4°C. Next, specimens were washed in 0.1 M sodium cacodylate buffer and treated with 1% osmium tetroxide (75632.5 mL, Sigma, Germany; v/v in 0.1 M sodium cacodylate buffer) for 1 h on ice followed by further sodium cacodylate buffer and distilled water washing steps. After the *en bloc* staining with 1% uranyl acetate (8473, Merck, Germany; v/v in distilled water) for 1 h on ice, samples were briefly washed in distilled water, dehydrated in an ascending concentration series of ethanol, infiltrated and embedded in epoxy resin (R1140, AGAR-100, Plano, Germany) to get finally polymerized for 48 h at 70°C. Subsequently, ultrathin sections (70–75 nm) from the cured resin blocks were cut with an Ultracut E microtome (Leica Microsystems, Germany) or an UC7 microtome (Leica Microsystems, Germany) equipped with a 35° diamond knife (Diatome AG, Biel, Switzerland) and mounted on 1% formvar-coated (w/v in water-free chloroform) copper slot grids (3.05 mm Ø, 1 mm × 2 mm; Plano, Germany). Before imaging these sections at 80 kV using a JEM1011 transmission electron microscope (JEOL, Germany), they were counterstained with uranyl acetate and Reynold's lead citrate (Reynolds, 1963) or uranyl acetate replacement solution (EMS, Science Services, United States). Micrographs of both hair cell types from the striolar and extrastriolar region were acquired at 10,000-x magnification with a Gatan Orius 1200A camera (Gatan GmbH, using the Digital Micrograph software package, United States).

Electron tomography

Electron tomography was utilized as described previously in Strenzke et al. (2016). Semithin sections (250 nm) were cut from conventionally embedded vestibular organs on an Ultracut E or an UC7 ultramicrotome (Leica Microsystems, Germany) with a 35° diamond knife (Diatome AG, Biel, Switzerland). Sections were placed on 1% formvar-coated (w/v in water-free chloroform) copper 100 mesh grids (3.05 mm Ø; Plano, Germany) and counterstained as described above. 10 nm gold beads (British Bio Cell, United Kingdom) were applied to both sides of the grids functioning as fiducial markers. With the Serial-EM software (Mastronarde, 2005), tilt series image acquisition was conducted mainly from −60 to +60° with 1° increments at 10,000-x magnification and a pixel size of 1.43 nm using a JEM2100 (JEOL, Germany) transmission electron microscope at 200 kV with a Gatan Orius 1200 A camera (Gatan Inc., United States). For final tomogram alignments, the IMOD software package etomo was used and tomographic reconstructions were generated using 3dmod (Kremer et al., 1996). Movies were generated with IMOD, Fiji (Schindelin et al., 2012) and Windows Movie Maker 2012.

Focused ion beam (FIB)-scanning electron microscopy (SEM)

Enhanced *en bloc* staining for FIB-SEM samples was performed according to Deerinck et al. (2018). After fixation (similar to the above-described conventional embedding protocol), utricular organs were treated with a 1.5% potassium ferrocyanide (EMS, United States) and 4% osmium tetroxide solution (v/v in 0.1 M sodium cacodylate buffer) for 1 h on ice. Next, specimens were briefly washed in distilled water and placed in a thiocarbohydrazide (w/v in distilled water) solution for 20 min followed by additional washing steps in distilled water. A second exposure to 2% osmium tetroxide (v/v in 0.1 M sodium cacodylate buffer) was conducted followed by brief washing steps in distilled water before the samples were placed in 2.5% uranyl acetate (v/v in distilled water) overnight at dark. Subsequently, samples were washed in distilled water and contrasted with Reynold's lead citrate (Reynolds, 1963) for 30 min at 60°C to be finally washed once again in distilled water, dehydrated in increasing ethanol concentrations, infiltrated and embedded in Durcupan (25%, 50%, 75% Durcupan in acetone for 1 h each and 100% Durcupan overnight; 44610, Sigma, Germany) to get polymerized for 48 h at 60°C. After trimming the cured blocks with a 90° diamond trimming knife (Diatome AG, Biel, Switzerland), the blocks were attached to SEM stubs (Science Services GmbH, Pin 12.7 mm × 3.1 mm) with a silver filled epoxy (Epoxy Conductive Adhesive, EPO-TEK EE 129–4; EMS, United States) and polymerized at 60° overnight. Samples were coated with a 10 nm platinum layer using the sputter coating machine EM ACE600 (Leica, Germany) at 30 mA current to be finally placed into the Crossbeam 540 focused ion beam scanning electron microscope (Carl Zeiss Microscopy GmbH, Germany) and positioned at an angle of 54°. A 400 nm platinum layer was deposited on top of the regions of interest and the Atlas 3D (Atlas

5.1, Fibics, Canada) software was used to collect the 3D data. Specimens were exposed to the ion beam driven with a 15 or 30 nA current while a 7 or 15 nA current was applied to polish the cross-section. Images from both hair cell types of the striolar and extrastriolar region were acquired at 1.5 kV using the ESB detector (450 or 1500 V ESB grid, pixel size x/y 3 or 5 nm) in a continuous mill and acquire mode using 700 pA or 1.5 nA for the milling aperture (z-step 5 nm). For subsequent post processing, data were aligned using the Plugin "Linear Stack Alignment with SIFT", inverted and cropped in Fiji. Depending on the dataset properties, a smoothing function (3 × 3), local contrast enhancement using a CLAHE plugin in Fiji, and a binning by 2 in x/y was applied (Schindelin et al., 2012). Movies were generated with IMOD (Kremer et al., 1996), Fiji, Blender (www.blender.org) and Windows Movie Maker 2012.

Nanoscale secondary ion mass spectrometry (NanoSIMS)

Mice were habituated to unlabeled ^{14}N-SILAM diet for 1 week before labeling (Silantes, Germany; cat. Num. 231, 004, 650). 10 and 14 months old C57BL/6JRj mice were then labeled with the ^{15}N-SILAM diet (Silantes, Germany; cat. Num. 231,304,650), for 14 or 21 days before the inner ear perfusion with a 4% paraformaldehyde (0335.1, Carl Roth, Germany) and 0.5% glutaraldehyde (G7651, Sigma, Germany) in PBS (P4417, Sigma, Germany; pH 7.4) fixative for 1 h on ice. Afterwards, inner ears were placed in a second fixative solution overnight at 4°C [2% glutaraldehyde in 0.1 M sodium cacodylate buffer (v/v, pH 7.2)]. On the second day fixed utricular organs were excised and the conventional embedding protocol was performed as described earlier in detail. The epoxy resin (R1140, AGAR-100, Plano, Germany) embedded samples were, similar to other conventional embedded specimens, further processed for transmission electron microscopy. 110 nm sections were cut using a 35° diamond knife (Diatome AG, Biel, Switzerland) with an UC7 ultramicrotome (Leica Microsystems, Germany) and placed on 200-mesh copper finder grids (01910-F, Ted Pella). Regions of interest (ROIs) were selected with a JEM1011 (JEOL, Germany) at 80 kV using different magnifications (×80, x150x, x800, x2,500, x6,000, x8,000) with a Gatan Orius 1200 A camera (Gatan Inc., United States). Subsequently, NanoSIMS imaging was performed. The areas of interest, previously imaged by TEM, were imaged with a NanoSIMS 50 L (Cameca, Gennevilliers Cedex, France) using an 8 kV Cs^{+133} primary ion source. To reach the steady-state of the secondary ion yield, prior to each measurement, an area of 100 × 100 µm was implanted applying a current of 50 pA for ~3 min (primary aperture D1:1). Subsequently, a primary ion current of ~0.25 pA (primary aperture D1:5) was applied to obtain images of 256 × 256 pixels from areas of 10 × 10 or 5 × 5 µm, resulting in a pixel size of 39.06 or 19.53 nm respectively. The dwell time was 5 m per pixel and three consecutive layers were accumulated for each final image. The detectors were set to collect the following ions: $^{12}C^{14}N^-$, $^{12}C^{15}N^-$, $^{31}P^-$ and $^{32}S^-$, and the mass resolving power of the instrument was adjusted to ensure the discrimination between isobaric interferences such as $^{12}C^{15}N^-$ from $^{13}C^{14}N^-$, or $^{12}C^{14}N^-$ from $^{12}C_2{}^1H_2{}^-$ by using an entrance slit of 20 × 140 µm and an aperture slit of 200 × 200 µm. The images were then exported and processed using WinImage (Cameca, Gennevilliers Cedex, France). The following masses were collected for each run: $^{12}C^{14}N$ (referred to as ^{14}N in this report), $^{12}C^{15}N$ (referred to as ^{15}N in this report), and ^{31}P. ^{31}P peak was used to mark the location of cellular structures. Each image shown in this manuscript is the result of a summation of all three image layers taken during analysis.

Data analysis and statistics

Quantitative analysis of electron microscopic random 2D sections was performed with ImageJ/Fiji (Schindelin et al., 2012) as follows:

In order to quantify the occurrence of floating ribbons, we defined "floating ribbons" by a lack of any physical contact to the presynaptic density, while an "attached ribbon" exhibited a clear membrane anchorage via a presynaptic density. For the ribbon size of attached ribbon synapses, the height and width were measured taking the longest axis of the ribbon excluding the presynaptic density as well as manual tracing of the synaptic ribbon was performed in order to determine the ribbon area. In contrast, due to the lack of an attachment of floating ribbons to the membrane, no precise ribbon orientation could be identified and hence the size of floating ribbons could only be analyzed by measuring the ribbon area.

For SVs of attached and floating ribbons, first the total amount of vesicles ≤80 nm from the ribbon surface were quantified in number and size. The latter analysis included the horizontal and vertical axis measurements, which were averaged to calculate the mean SV diameter. Next, the SV density was calculated by dividing the total number of SVs by the ribbon surface area.

Exclusively for attached ribbon synapses, two distinct morphological vesicle pools were additionally quantified in terms of numbers [as previously characterized in (Strenzke et al., 2016)]: (i) membrane-proximal synaptic vesicles (MP-SVs, ≤25 nm distance between SV membrane and AZ membrane and ≤80 nm from the presynaptic density); and (ii) ribbon-associated synaptic vesicles (RA-SVs, first layer of vesicles around the ribbon with a maximum distance of 80 nm from the ribbon surface to the vesicle membrane and not falling into the MP-SV pool).

Quantitative analysis of FIB-SEM data

FIB-SEM datasets were segmented semi-automatically using the 3dmod package from the IMOD software (Kremer et al., 1996) and applying the imodinfo function, information about the ribbon and mitochondria volume was given. Distance measurements were performed with the measurement drawing tool along the *x*, *y* and *z*-axis.

Quantitative analysis of NanoSIMS data

NanoSIMS images were analyzed using a custom-written Matlab macro (the Mathworks Inc., Natick, MA, United States). NanoSIMS images were overlaid with the EM images, using Adobe Photoshop CS6 (Adobe Systems Incorporated). ROIs were selected manually on

the EM images, and the ^{15}N and ^{14}N counts were measured for all ROIs in the respective NanoSIMS images. The results were saved as text files and were then combined to provide the statistics shown in the NanoSIMS figure.

All data are mainly presented as boxplots with individual data points overlaid and as bar graphs highlighting the mean or percentages of the data, which were analyzed using Excel, Igor Pro 6 (Wavemetrics Inc., United States), R and Java, if not otherwise indicated. Normality was assessed with the Jarque-Bera test and equality of variances in normally distributed data was assessed with the F-test. In order to compare two samples, the two-tailed unpaired Student's t-test, or, when data were not normally distributed and/or variance was unequal between samples, the unpaired two-tailed Mann-Whitney-Wilcoxon test was used. One-way ANOVA test (followed by Fischer *post hoc* tests (NanoSIMS data)) followed by Tukey's test was used to calculate statistical significance in multiple comparisons for normally distributed data or in case of non-normally distributed data the Kruskal-Wallis (KW) test followed by non-parametric multiple comparisons test (NPMC) was used.

Employing the analysis tool based on Java Statistical Classes library (JSC) (Bertie, 2002) applied in our previous study (Jean et al., 2018), we performed the KW test for the identification of significant differences between SV diameters. Non-significant differences between samples are indicated as *n. s.*, significant differences are indicated as $^{*}p < 0.05$, $^{**}p < 0.01$, $^{***}p < 0.001$, $^{****}p < 0.0001$. Affinity Designer 1.10.5 and Adobe Illustrator 2023 (Adobe Inc., United States) were utilized for Figure assembling and display.

Data availability statement

The original contributions presented in the study are included in the article/Supplementary Material, further inquiries can be directed to the corresponding authors.

Ethics statement

The animal study was reviewed and approved by University of Göttingen Board for Animal Welfare and the Animal Welfare Office of the State of Lower Saxony.

Author contributions

SM and CW designed the study. SM performed electron microscopic work (conventional embeddings, enhanced *en bloc* stainings, TEM of random sections, electron tomography, FIB-SEM). TH contributed to 2D TEM data analysis and acquisition. TP, MM, and CV performed immunohistochemistry as well as confocal microscopy and STED. SM, MG, TH, MM, and CV analyzed data. AMS performed and WM supervised FIB-SEM. MG contributed to statistical analysis. PI made the Blender movies. SJ and PI contributed to mitochondria data interpretation. EFF prepared mice for the NanoSIMS experiments. SM and EFF prepared tissue samples for NanoSIMS. CW performed TEM image acquisitions for NanoSIMS. PAG and KG performed NanoSIMS and SOR and PAG analyzed NanoSIMS data. SM and CW prepared the manuscript with contributions from all other authors. All authors contributed to the article and approved the submitted version.

Funding

This work was funded by German Research Foundation grants (Deutsche Forschungsgemeinschaft): Collaborative Research Center 889 [Projects A07 (CW), B08 to CV, and B09 to TP] and TP, SJ, WM, and CW were further supported by the Deutsche Forschungsgemeinschaft under Germany's Excellence Strategy–EXC 2067/1-390729940. SOR, SJ, and CW were further funded by German Research Foundation grants: Collaborative Research Center 1286 [Projects A04 to CW, A05 to SJ, and A03 to SOR]. Part of this work (AMS) was funded by the Cluster of Excellence and DFG Research Center Nanoscale Microscopy and Molecular Physiology of the Brain [Research field A1 (WM)] and by the Deutsche Forschungsgemeinschaft (DFG) (FOR2848, MO 1082/1-2, project 08 to WM). CV was an Otto Creutzfeldt-Fellow of the Elisabeth and Helmut Uhl Foundation. MM and TP are funded via the BMBF and MWK (Bundesministerium für Bildung und Forschung and Niedersächsisches Ministerium für Wissenschaft und Kultur; Professorinnenprogramm III, 22-38 285/1-3-12-1 and 22-76251-99-17/19 to TP). EFF was supported by a Schram Stiftung (T0287/35359/2020) and a DFG grant (FO 1342/1-3). SOR, KG, and PAG were supported by a DFG grant (RI 1967/10-1, NeuroNex). The position of SM was partially paid by a grant of the "Niedersächsisches Vorab" to Tobias Moser.

Acknowledgments

We thank S. Gerke, C. Senger-Freitag, A. J. Goldak, S. Langer, I. Preuss, C. Fischer, A. Zeise, and C. Förster for expert technical assistance, O. L. Diaz for IT support.

Conflict of interest

The authors declare that the research was conducted in the absence of any commercial or financial relationships that could be construed as a potential conflict of interest.

Publisher's note

Supplementary material

The Supplementary Material for this article can be found online at: https://www.frontiersin.org/articles/10.3389/fcell.2023.1178992/full#supplementary-material

References

Agrawal, Y., Carey, J. P., Della Santina, C. C., Schubert, M. C., and Minor, L. B. (2009). Disorders of balance and vestibular function in US adults: data from the national health and nutrition examination survey, 2001-2004. *Arch. Intern. Med.* 169, 938–944. doi:10.1001/archinternmed.2009.66

Agrawal, Y., Zuniga, M. G., Davalos-Bichara, M., Schubert, M. C., Walston, J. D., Hughes, J., et al. (2012). Decline in semicircular canal and otolith function with age. *Otol. Neurotol.* 33, 832–839. doi:10.1097/MAO.0b013e3182545061

Bermúdez Rey, M. C., Clark, T. K., Wang, W., Leeder, T., Bian, Y., and Merfeld, D. M. (2016). Vestibular perceptual thresholds increase above the age of 40. *Front. Neurol.* 7, 162. doi:10.3389/fneur.2016.00162

Bertie, A. (2002). Java applications for teaching statistics. *MSOR Connect.* 2, 78–81. doi:10.11120/msor.2002.02030078

Böttger, E. C., and Schacht, J. (2013). The mitochondrion: a perpetrator of acquired hearing loss. *Hear. Res.* 303, 12–19. doi:10.1016/j.heares.2013.01.006

Burns, J. C., and Stone, J. S. (2017). Development and regeneration of vestibular hair cells in mammals. *Semin. Cell Dev. Biol.* 65, 96–105. doi:10.1016/j.semcdb.2016.11.001

Chakrabarti, R., Michanski, S., and Wichmann, C. (2018). Vesicle sub-pool organization at inner hair cell ribbon synapses. *EMBO Rep.* 19, e44937. doi:10.15252/embr.201744937

Contini, D., Holstein, G. R., and Art, J. J. (2020). Synaptic cleft microenvironment influences potassium permeation and synaptic transmission in hair cells surrounded by calyx afferents in the turtle. *J. Physiol.* 598, 853–889. doi:10.1113/JP278680

Cserép, C., Pósfai, B., Schwarcz, A. D., and Dénes, Á. (2018). Mitochondrial ultrastructure is coupled to synaptic performance at axonal release sites. *eNeuro* 5, ENEURO.0390-17.2018. doi:10.1523/ENEURO.0390-17.2018

Curthoys, I. S. (1979). The development of function of horizontal semicircular canal primary neurons in the rat. *Brain Res.* 167, 41–52. doi:10.1016/0006-8993(79)90261-0

Dechesne, C., Mbiene, J. P., and Sans, A. (1986). Postnatal development of vestibular receptor surfaces in the rat. *Acta Otolaryngol. (Stockh.)* 101, 11–18. doi:10.3109/00016488609108602

Deerinck, T. J., Shone, T. M., Bushong, E. A., Ramachandra, R., Peltier, S. T., and Ellisman, M. H. (2018). High-performance serial block-face SEM of nonconductive biological samples enabled by focal gas injection-based charge compensation. *J. Microsc.* 270, 142–149. doi:10.1111/jmi.12667

Devine, M. J., and Kittler, J. T. (2018). Mitochondria at the neuronal presynapse in health and disease. *Nat. Rev. Neurosci.* 19, 63–80. doi:10.1038/nrn.2017.170

Dick, O., tom Dieck, S., Altrock, W. D., Ammermüller, J., Weiler, R., Garner, C. C., et al. (2003). The presynaptic active zone protein bassoon is essential for photoreceptor ribbon synapse formation in the retina. *Neuron* 37, 775–786. doi:10.1016/s0896-6273(03)00086-2

Druckenbrod, N. R., and Goodrich, L. V. (2015). Sequential retraction segregates SGN processes during target selection in the cochlea. *J. Neurosci.* 35, 16221–16235. doi:10.1523/JNEUROSCI.2236-15.2015

Eatock, R. A., and Lysakowski, A. (2006). "Mammalian vestibular hair cells," in *Vertebrate hair cells*. Editors R. A. Eatock, R. R. Fay, and A. N. Popper (New York, NY: Springer), 348–442.

Eatock, R. A., Rüsch, A., Lysakowski, A., and Saeki, M. (1998). Hair cells in mammalian utricles. *Otolaryngol. Neck Surg.* 119, 172–181. doi:10.1016/S0194-5998(98)70052-X

Eatock, R. A. (2018). Specializations for fast signaling in the amniote vestibular inner ear. *Integr. Comp. Biol.* 58, 341–350. doi:10.1093/icb/icy069

Engström, H., Bergström, B., and Ades, H. W. (1972). Macula utriculi and macula sacculi in the squirrel monkey. *Acta oto-laryngol. Suppl.* 301, 75–71. doi:10.3109/00016487209122691

Esterberg, R., Linbo, T., Pickett, S. B., Wu, P., Ou, H. C., Rubel, E. W., et al. (2016). Mitochondrial calcium uptake underlies ROS generation during aminoglycoside-induced hair cell death. *J. Clin. Invest.* 126, 3556–3566. doi:10.1172/JCI84939

Favre, D., Dememes, D., and Sans, A. (1986). Microtubule organization and synaptogenesis in the vestibular sensory cells. *Dev. Brain Res.* 25, 137–142. doi:10.1016/0165-3806(86)90161-6

Favre, D., and Sans, A. (1979). Morphological changes in afferent vestibular hair cell synapses during the postnatal development of the cat. *J. Neurocytol.* 8, 765–775. doi:10.1007/BF01206675

Fischel-Ghodsian, N., Kopke, R. D., and Ge, X. (2004). Mitochondrial dysfunction in hearing loss. *Mitochondrion* 4, 675–694. doi:10.1016/j.mito.2004.07.040

Forgac, M. (2007). Vacuolar ATPases: rotary proton pumps in physiology and pathophysiology. *Nat. Rev. Mol. Cell Biol.* 8, 917–929. doi:10.1038/nrm2272

Forge, A., Li, L., Corwin, J. T., and Nevill, G. (1993). Ultrastructural evidence for hair cell regeneration in the mammalian inner ear. *Science* 259, 1616–1619. doi:10.1126/science.8456284

Forge, A., Li, L., and Nevill, G. (1998). Hair cell recovery in the vestibular sensory epithelia of mature Guinea pigs. *J. Comp. Neurol.* 397, 69–88. doi:10.1002/(sici)1096-9861(19980720)397:1<69:aid-cne6>3.0.co;2-g

Fuchs, M., Sendelbeck, A., Atorf, J., Kremers, J., and Brandstätter, J. H. (2013). Strain differences in illumination-dependent structural changes at mouse photoreceptor ribbon synapses. *J. Comp. Neurol.* 521, 69–78. doi:10.1002/cne.23161

Goldberg, J. M., Lysakowski, A., and Fernández, C. (1990). Morphophysiological and ultrastructural studies in the mammalian cristae ampullares. *Hear. Res.* 49, 89–102. doi:10.1016/0378-5955(90)90097-9

Goldberg, J. M., Lysakowski, A., and Fernández, C. (1992). Structure and function of vestibular nerve fibers in the chinchilla and squirrel monkey. *Ann. N. Y. Acad. Sci.* 656, 92–107. doi:10.1111/j.1749-6632.1992.tb25202.x

Golub, J. S., Tong, L., Ngyuen, T. B., Hume, C. R., Palmiter, R. D., Rubel, E. W., et al. (2012). Hair cell replacement in adult mouse utricles after targeted ablation of hair cells with diphtheria toxin. *J. Neurosci.* 32, 15093–15105. doi:10.1523/JNEUROSCI.1709-12.2012

Hård, E., and Larsson, K. (1975). Development of air righting in rats. *Brain. Behav. Evol.* 11, 53–59. doi:10.1159/000123624

Harris, J. J., Jolivet, R., and Attwell, D. (2012). Synaptic energy use and supply. *Neuron* 75, 762–777. doi:10.1016/j.neuron.2012.08.019

Henry, K. R., and Chole, R. A. (1980). Genotypic differences in behavioral, physiological and anatomical expressions of age-related hearing loss in the laboratory mouse. *Audiology* 19, 369–383. doi:10.3109/00206098009070071

Hequembourg, S., and Liberman, M. C. (2001). Spiral ligament Pathology: a major aspect of age-related cochlear degeneration in C57bl/6 mice. *J. Assoc. Res. Otolaryngol.* 2, 118–129. doi:10.1007/s101620010075

Heywood, P., Van de Water, T. R., Hilding, D. A., and Ruben, R. J. (1975). Distribution of microtubules and microfilaments in developing vestibular sensory epithelium of mouse otocysts grown *in vitro*. *J. Cell Sci.* 17, 171–189. doi:10.1242/jcs.17.1.171

Hicks, K. L., Wisner, S. R., Cox, B. C., and Stone, J. S. (2020). Atoh1 is required in supporting cells for regeneration of vestibular hair cells in adult mice. *Hear. Res.* 385, 107838. doi:10.1016/j.heares.2019.107838

Highstein, S. M., Mann, M. A., Holstein, G. R., and Rabbitt, R. D. (2015). The quantal component of synaptic transmission from sensory hair cells to the vestibular calyx. *J. Neurophysiol.* 113, 3827–3835. doi:10.1152/jn.00055.2015

Huang, L.-C., Barclay, M., Lee, K., Peter, S., Housley, G. D., Thorne, P. R., et al. (2012). Synaptic profiles during neurite extension, refinement and retraction in the developing cochlea. *Neural Dev.* 7, 38–17. doi:10.1186/1749-8104-7-38

Ison, J. R., and Allen, P. D. (2003). Low-frequency tone pips elicit exaggerated startle reflexes in C57bl/6J mice with hearing loss. *J. Assoc. Res. Otolaryngol.* 4, 495–504. doi:10.1007/s10162-002-3046-2

Iwasaki, S., Egami, N., Fujimoto, C., Chihara, Y., Ushio, M., Kashio, A., et al. (2011). The mitochondrial A3243G mutation involves the peripheral vestibule as well as the cochlea. *Laryngoscope* 121, 1821–1824. doi:10.1002/lary.21879

Iwasaki, S., Smulders, Y. E., Burgess, A. M., McGarvie, L. A., MacDougall, H. G., Halmagyi, G. M., et al. (2008). Ocular vestibular evoked myogenic potentials to bone conducted vibration of the midline forehead at Fz in healthy subjects. *Clin. Neurophysiol.* 119, 2135–2147. doi:10.1016/j.clinph.2008.05.028

Jamon, M. (2014). The development of vestibular system and related functions in mammals: impact of gravity. *Front. Integr. Neurosci.* 8, 11. doi:10.3389/fnint.2014.00011

Jean, P., Morena, D. L., Michanski, S., Tobón, L. M. J., Chakrabarti, R., Picher, M. M., et al. (2018). The synaptic ribbon is critical for sound encoding at high rates and with temporal precision. *eLife* 7, e29275. doi:10.7554/eLife.29275

Johnson, K. R., Erway, L. C., Cook, S. A., Willott, J. F., and Zheng, Q. Y. (1997). A major gene affecting age-related hearing loss in C57BL/6J mice. *Hear. Res.* 114, 83–92. doi:10.1016/s0378-5955(97)00155-x

Kawamoto, K., Izumikawa, M., Beyer, L. A., Atkin, G. M., and Raphael, Y. (2009). Spontaneous hair cell regeneration in the mouse utricle following gentamicin ototoxicity. *Hear. Res.* 247, 17–26. doi:10.1016/j.heares.2008.08.010

Kawamura, N., Ito, M., and Seto-Ohshima, A. (1998). Postnatal development of the structure of the peripheral vestibular system of the gerbil. *ACTA histochem. cytochem.* 31, 33–38. doi:10.1267/ahc.31.33

Khimich, D., Nouvian, R., Pujol, R., tom Dieck, S., Egner, A., Gundelfinger, E. D., et al. (2005). Hair cell synaptic ribbons are essential for synchronous auditory signalling. *Nature* 434, 889–894. doi:10.1038/nature03418

Kokotas, H., Petersen, M., and Willems, P. (2007). Mitochondrial deafness. *Clin. Genet.* 71, 379–391. doi:10.1111/j.1399-0004.2007.00800.x

Koundakjian, E. J., Appler, J. L., and Goodrich, L. V. (2007). Auditory neurons make stereotyped wiring decisions before maturation of their targets. *J. Neurosci. Off. J. Soc. Neurosci.* 27, 14078–14088. doi:10.1523/JNEUROSCI.3765-07.2007

Kremer, J. R., Mastronarde, D. N., and McIntosh, J. R. (1996). Computer visualization of three-dimensional image data using IMOD. *J. Struct. Biol.* 116, 71–76. doi:10.1006/jsbi.1996.0013

Lannou, J., Precht, W., and Cazin, L. (1979). The postnatal development of functional properties of central vestibular neurons in the rat. *Brain Res.* 175, 219–232. doi:10.1016/0006-8993(79)91002-3

Lenzi, D., Crum, J., Ellisman, M. H., and Roberts, W. M. (2002). Depolarization redistributes synaptic membrane and creates a gradient of vesicles on the synaptic body at a ribbon synapse. *Neuron* 36, 649–659. doi:10.1016/s0896-6273(02)01025-5

Lenzi, D., Runyeon, J. W., Crum, J., Ellisman, M. H., and Roberts, W. M. (1999). Synaptic vesicle populations in saccular hair cells reconstructed by electron tomography. *J. Neurosci.* 19, 119–132. doi:10.1523/JNEUROSCI.19-01-00119.1999

Li, H.-S., and Borg, E. (1991). Age-related loss of auditory sensitivity in two mouse genotypes. *Acta Otolaryngol. (Stockh.)* 111, 827–834. doi:10.3109/00016489109138418

Li, W., You, D., Chen, Y., Chai, R., and Li, H. (2016). Regeneration of hair cells in the mammalian vestibular system. *Front. Med.* 10, 143–151. doi:10.1007/s11684-016-0451-1

Liberman, M. C. (1980). Morphological differences among radial afferent fibers in the cat cochlea: an electron-microscopic study of serial sections. *Hear. Res.* 3, 45–63. doi:10.1016/0378-5955(80)90007-6

Lin, V., Golub, J. S., Nguyen, T. B., Hume, C. R., Oesterle, E. C., and Stone, J. S. (2011). Inhibition of notch activity promotes nonmitotic regeneration of hair cells in the adult mouse utricles. *J. Neurosci.* 31, 15329–15339. doi:10.1523/JNEUROSCI.2057-11.2011

Lysakowski, A., and Goldberg, J. M. (1997). A regional ultrastructural analysis of the cellular and synaptic architecture in the chinchilla cristae ampullares. *J. Comp. Neurol.* 389, 419–443. doi:10.1002/(sici)1096-9861(19971222)389:3<419:aid-cne5>3.0.co;2-3

Lysakowski, A., and Goldberg, J. M. (2008). Ultrastructural analysis of the cristae ampullares in the squirrel monkey (*Saimiri sciureus*). *J. Comp. Neurol.* 511, 47–64. doi:10.1002/cne.21827

Lysakowski, A. (1996). Synaptic organization of the crista ampullaris in vertebrates. *Ann. N. Y. Acad. Sci.* 781, 164–182. doi:10.1111/j.1749-6632.1996.tb15700.x

Madisen, L., Zwingman, T. A., Sunkin, S. M., Oh, S. W., Zariwala, H. A., Gu, H., et al. (2010). A robust and high-throughput Cre reporting and characterization system for the whole mouse brain. *Nat. Neurosci.* 13, 133–140. doi:10.1038/nn.2467

Magupalli, V. G., Schwarz, K., Alpadi, K., Natarajan, S., Seigel, G. M., and Schmitz, F. (2008). Multiple RIBEYE-RIBEYE interactions create a dynamic scaffold for the formation of synaptic ribbons. *J. Neurosci.* 28, 7954–7967. doi:10.1523/JNEUROSCI.1964-08.2008

Mastronarde, D. N. (2005). Automated electron microscope tomography using robust prediction of specimen movements. *J. Struct. Biol.* 152, 36–51. doi:10.1016/j.jsb.2005.07.007

Matthews, G., and Fuchs, P. (2010). The diverse roles of ribbon synapses in sensory neurotransmission. *Nat. Rev. Neurosci.* 11, 812–822. doi:10.1038/nrn2924

Michanski, S., Smaluch, K., Steyer, A. M., Chakrabarti, R., Setz, C., Oestreicher, D., et al. (2019). Mapping developmental maturation of inner hair cell ribbon synapses in the apical mouse cochlea. *Proc. Natl. Acad. Sci.* 116, 6415–6424. doi:10.1073/pnas.1812029116

Mikaelian, D. O., Warfield, D., and Norris, O. (1974). Genetic progressive hearing loss in the C57-b16 mouse. Relation of behavioral responses to chochlear anatomy. *Acta Otolaryngol. (Stockh.)* 77, 327–334. doi:10.3109/00016487409124632

Mock, B. E., Vijayakumar, S., Pierce, J., Jones, T. A., and Jones, S. M. (2016). Differential effects of Cdh23753A on auditory and vestibular functional aging in C57bl/6J mice. *Neurobiol. Aging* 43, 13–22. doi:10.1016/j.neurobiolaging.2016.03.013

Moser, T., Brandt, A., and Lysakowski, A. (2006). Hair cell ribbon synapses. *Cell Tissue Res.* 326, 347–359. doi:10.1007/s00441-006-0276-3

Moser, T., Grabner, C. P., and Schmitz, F. (2019). Sensory processing at ribbon synapses in the retina and the cochlea. *Physiol. Rev.* 100, 103–144. doi:10.1152/physrev.00026.2018

Mukhopadhyay, M., and Pangrsic, T. (2022). Synaptic transmission at the vestibular hair cells of amniotes. *Mol. Cell. Neurosci.* 121, 103749. doi:10.1016/j.mcn.2022.103749

Neuhauser, H. K. (2007). Epidemiology of vertigo. *Curr. Opin. Neurol.* 20, 40–46. doi:10.1097/WCO.0b013e328013f432

Neuhauser, H. K., von Brevern, M., Radtke, A., Lezius, F., Feldmann, M., Ziese, T., et al. (2005). Epidemiology of vestibular vertigo: a neurotologic survey of the general population. *Neurology* 65, 898–904. doi:10.1212/01.wnl.0000175987.59991.3d

Nordemar, H. (1983). Postnatal development of the vestibular sensory epithelium in the mouse. *Acta Otolaryngol. (Stockh.)* 96, 447–456. doi:10.3109/00016488309132731

Park, J. C., Hubel, S. B., and Woods, A. D. (1987). Morphometric analysis and fine structure of the vestibular epithelium of aged C57BL/6NNia mice. *Hear. Res.* 28, 87–96. doi:10.1016/0378-5955(87)90156-0

Pathak, D., Shields, L. Y., Mendelsohn, B. A., Haddad, D., Lin, W., Gerencser, A. A., et al. (2015). The role of mitochondrially derived ATP in synaptic vesicle recycling. *J. Biol. Chem.* 290, 22325–22336. doi:10.1074/jbc.M115.656405

Peineau, T., Belleudy, S., Pietropaolo, S., Bouleau, Y., and Dulon, D. (2021). Synaptic release potentiation at aging auditory ribbon synapses. *Front. Aging Neurosci.* 13, 756449. doi:10.3389/fnagi.2021.756449

Pickett, S. B., Thomas, E. D., Sebe, J. Y., Linbo, T., Esterberg, R., Hailey, D. W., et al. (2018). Cumulative mitochondrial activity correlates with ototoxin susceptibility in zebrafish mechanosensory hair cells. *eLife* 7, e38062. doi:10.7554/eLife.38062

Piker, E. G., Jacobson, G. P., McCaslin, D. L., and Hood, L. J. (2011). Normal characteristics of the ocular vestibular evoked myogenic potential. *J. Am. Acad. Audiol.* 22, 222–230. doi:10.3766/jaaa.22.4.5

Rangaraju, V., Calloway, N., and Ryan, T. A. (2014). Activity-driven local ATP synthesis is required for synaptic function. *Cell* 156, 825–835. doi:10.1016/j.cell.2013.12.042

Requena, T., Espinosa-Sanchez, J. M., and Lopez-Escamez, J. A. (2014). Genetics of dizziness: cerebellar and vestibular disorders. *Curr. Opin. Neurol.* 27, 98–104. doi:10.1097/WCO.0000000000000053

Reynolds, E. S. (1963). The use of lead citrate at high ph as an electron-opaque stain in electron microscopy. *J. Cell Biol.* 17, 208–212. doi:10.1083/jcb.17.1.208

Rosengren, S. M., Govender, S., and Colebatch, J. G. (2011). Ocular and cervical vestibular evoked myogenic potentials produced by air- and bone-conducted stimuli: comparative properties and effects of age. *Clin. Neurophysiol.* 122, 2282–2289. doi:10.1016/j.clinph.2011.04.001

Ross, M. D. (1994). A spaceflight study of synaptic plasticity in adult rat vestibular maculas. *Acta Otolaryngol. (Stockh.)* 114, 3–14. doi:10.3109/00016489409124327

Ross, M. D. (2000). Changes in ribbon synapses and rough endoplasmic reticulum of rat utricular macular hair cells in weightlessness. *Acta Otolaryngol. (Stockh.)* 120, 490–499. doi:10.1080/000164800750045983

Rossoll, W., and Bassell, G. J. (2019). Crosstalk of local translation and mitochondria: powering plasticity in axons and dendrites. *Neuron* 101, 204–206. doi:10.1016/j.neuron.2018.12.027

Rüsch, A., Lysakowski, A., and Eatock, R. A. (1998). Postnatal development of type I and type II hair cells in the mouse utricle: acquisition of voltage-gated conductances and differentiated morphology. *J. Neurosci.* 18, 7487–7501. doi:10.1523/JNEUROSCI.18-18-07487.1998

Rutherford, M. A., and Moser, T. (2016). "The ribbon synapse between type I spiral ganglion neurons and inner hair cells," in *The primary auditory neurons of the mammalian cochlea*. Editors A. Dabdoub, B. Fritzsch, A. N. Popper, and R. R. Fay (New York, NY: Springer), 117–156.

Sadeghi, S. G., Pyott, S. J., Yu, Z., and Glowatzki, E. (2014). Glutamatergic signaling at the vestibular hair cell calyx synapse. *J. Neurosci.* 34, 14536–14550. doi:10.1523/JNEUROSCI.0369-13.2014

Sans, A., and Scarfone, E. (1996). Afferent calyces and type I hair cells during development. A new morphofunctional hypothesis. *Ann. N. Y. Acad. Sci.* 781, 1–12. doi:10.1111/j.1749-6632.1996.tb15688.x

Schindelin, J., Arganda-Carreras, I., Frise, E., Kaynig, V., Longair, M., Pietzsch, T., et al. (2012). Fiji: an open-source platform for biological-image analysis. *Nat. Methods* 9, 676–682. doi:10.1038/nmeth.2019

Shnerson, A., and Pujol, R. (1981). Age-related changes in the C57BL/6J mouse cochlea. I. Physiological findings. *Dev. Brain Res.* 2, 65–75. doi:10.1016/0165-3806(81)90059-6

Shone, G., Altschuler, R. A., Miller, J. M., and Nuttall, A. L. (1991). The effect of noise exposure on the aging ear. *Hear. Res.* 56, 173–178. doi:10.1016/0378-5955(91)90167-8

Sjöbäck, D. B., and Gulley, R. L. (1979). Synaptic structures in the type ii hair cell in the vestibular system of the Guinea pig: *a freeze-fracture and TEM study*. *Acta Otolaryngol. (Stockh.)* 88, 401–411. doi:10.3109/00016487909137185

Slowik, A. D., and Bermingham-McDonogh, O. (2013). Hair cell generation by notch inhibition in the adult mammalian cristae. *JARO J. Assoc. Res. Otolaryngol.* 14, 813–828. doi:10.1007/s10162-013-0414-z

Smith, H. L., Bourne, J. N., Cao, G., Chirillo, M. A., Ostroff, L. E., Watson, D. J., et al. (2016). Mitochondrial support of persistent presynaptic vesicle mobilization with age-dependent synaptic growth after LTP. *eLife* 5, e15275. doi:10.7554/eLife.15275

Sobkowicz, H. M., Rose, J. E., Scott, G. L., and Levenick, C. V. (1986). Distribution of synaptic ribbons in the developing organ of Corti. *J. Neurocytol.* 15, 693–714. doi:10.1007/BF01625188

Sobkowicz, H., Rose, J., Scott, G., and Slapnick, S. (1982). Ribbon synapses in the developing intact and cultured organ of Corti in the mouse. *J. Neurosci.* 2, 942–957. doi:10.1523/JNEUROSCI.02-07-00942.1982

Songer, J. E., and Eatock, R. A. (2013). Tuning and timing in mammalian type I hair cells and calyceal synapses. *J. Neurosci.* 33, 3706–3724. doi:10.1523/JNEUROSCI.4067-12.2013

Spaiardi, P., Marcotti, W., Masetto, S., and Johnson, S. L. (2022). Signal transmission in mature mammalian vestibular hair cells. *Front. Cell. Neurosci.* 16, 806913. doi:10.3389/fncel.2022.806913

Spiwoks-Becker, I., Glas, M., Lasarzik, I., and Vollrath, L. (2004). Mouse photoreceptor synaptic ribbons lose and regain material in response to illumination changes. *Eur. J. Neurosci.* 19, 1559–1571. doi:10.1111/j.1460-9568.2004.03198.x

Spongr, V. P., Flood, D. G., Frisina, R. D., and Salvi, R. J. (1997). Quantitative measures of hair cell loss in CBA and C57BL/6 mice throughout their life spans. *J. Acoust. Soc. Am.* 101, 3546–3553. doi:10.1121/1.418315

Stamataki, S., Francis, H. W., Lehar, M., May, B. J., and Ryugo, D. K. (2006). Synaptic alterations at inner hair cells precede spiral ganglion cell loss in aging C57BL/6J mice. *Hear. Res.* 221, 104–118. doi:10.1016/j.heares.2006.07.014

Sterling, P., and Matthews, G. (2005). Structure and function of ribbon synapses. *Trends Neurosci.* 28, 20–29. doi:10.1016/j.tins.2004.11.009

Strenzke, N., Chakrabarti, R., Al-Moyed, H., Müller, A., Hoch, G., Pangrsic, T., et al. (2016). Hair cell synaptic dysfunction, auditory fatigue and thermal sensitivity in otoferlin Ile515Thr mutants. *EMBO J.* 35, 2519–2535. doi:10.15252/embj.201694564

Sultemeier, D. R., Choy, K. R., Schweizer, F. E., and Hoffman, L. F. (2017). Spaceflight-induced synaptic modifications within hair cells of the mammalian utricle. *J. Neurophysiol.* 117, 2163–2178. doi:10.1152/jn.00240.2016

Thomas, C. I., Keine, C., Okayama, S., Satterfield, R., Musgrove, M., Guerrero-Given, D., et al. (2019). Presynaptic mitochondria volume and abundance increase during development of a high-fidelity synapse. *J. Neurosci.* 39, 7994–8012. doi:10.1523/JNEUROSCI.0363-19.2019

Verhage, M., and Sørensen, J. B. (2008). Vesicle docking in regulated exocytosis. *Traffic* 9, 1414–1424. doi:10.1111/j.1600-0854.2008.00759.x

Vincent, P. F. Y., Bouleau, Y., Safieddine, S., Petit, C., and Dulon, D. (2014). Exocytotic machineries of vestibular type I and cochlear ribbon synapses display similar intrinsic otoferlin-dependent Ca2+ sensitivity but a different coupling to Ca2+ channels. *J. Neurosci.* 34, 10853–10869. doi:10.1523/JNEUROSCI.0947-14.2014

Vollrath, L., and Seidel, A. (1989). The plasticity of synaptic ribbons. *Biomed. Res. Tokyo* 10, 207–212.

Voorn, R. A., and Vogl, C. (2020). Molecular assembly and structural plasticity of sensory ribbon synapses—a presynaptic perspective. *Int. J. Mol. Sci.* 21, 8758. doi:10.3390/ijms21228758

Vranceanu, F., Perkins, G. A., Terada, M., Chidavaenzi, R. L., Ellisman, M. H., and Lysakowski, A. (2012). Striated organelle, a cytoskeletal structure positioned to modulate hair-cell transduction. *Proc. Natl. Acad. Sci. U. S. A.* 109, 4473–4478. doi:10.1073/pnas.1101003109

Waagepetersen, H. S., Sonnewald, U., and Schousboe, A. (2003). Compartmentation of glutamine, glutamate, and GABA metabolism in neurons and astrocytes: functional implications. *Neurosci.* 9, 398–403. doi:10.1177/1073858403254006

Walton, J. P., Frisina, R. D., and Meierhans, L. R. (1995). Sensorineural hearing loss alters recovery from short-term adaptation in the C57BL/6 mouse. *Hear Res.* 88, 19–26. doi:10.1016/0378-5955(95)00093-j

Wan, G., Ji, L., Schrepfer, T., Gong, S., Wang, G.-P., and Corfas, G. (2019). Synaptopathy as a mechanism for age-related vestibular dysfunction in mice. *Front. Aging Neurosci.* 11, 156. doi:10.3389/fnagi.2019.00156

Wersall, J. (1956). Studies on the structure and innervation of the sensory epithelium of the cristae ampulares in the Guinea pig; a light and electron microscopic investigation. *Acta oto-laryngol. Suppl.* 126, 1–85.

White, J. A., Burgess, B. J., Hall, R. D., and Nadol, J. B. (2000). Pattern of degeneration of the spiral ganglion cell and its processes in the C57BL/6J mouse. *Hear. Res.* 141, 12–18. doi:10.1016/s0378-5955(99)00204-x

Willott, J. F. (1986). Effects of aging, hearing loss, and anatomical location on thresholds of inferior colliculus neurons in C57BL/6 and CBA mice. *J. Neurophysiol.* 56, 391–408. doi:10.1152/jn.1986.56.2.391

Willott, J. F., Parham, K., and Hunter, K. P. (1988b). Response properties of inferior colliculus neurons in middle-aged C57BL/6J mice with presbycusis. *Hear. Res.* 37, 15–27. doi:10.1016/0378-5955(88)90074-3

Willott, J. F., Parham, K., and Hunter, K. P. (1988a). Response properties of inferior colliculus neurons in young and very old CBA/J mice. *Hear. Res.* 37, 1–14. doi:10.1016/0378-5955(88)90073-1

Wong, A. B., Rutherford, M. A., Gabrielaitis, M., Pangršič, T., Göttfert, F., Frank, T., et al. (2014). Developmental refinement of hair cell synapses tightens the coupling of Ca2+ influx to exocytosis. *EMBO J.* 33, 247–264. doi:10.1002/embj.201387110

Wong, H. C., Zhang, Q., Beirl, A. J., Petralia, R. S., Wang, Y.-X., and Kindt, K. S. (2019). Synaptic mitochondria are critical for hair-cell synapse formation and function. *Dev. Biol.* doi:10.1101/671701

Woods, A. D., and Park, J. C. (1987). Persistence of synaptic bodies in saccular hair cells of senescent mice. *Acta Otolaryngol. (Stockh.)* 104, 193–201. doi:10.3109/00016488709107318

Yamashita, M., and Ohmori, H. (1991). Synaptic bodies and vesicles in the calix type synapse of chicken semicircular canal ampullae. *Neurosci. Lett.* 129, 43–46. doi:10.1016/0304-3940(91)90716-7

Yao, J., and Bajjalieh, S. M. (2008). Synaptic vesicle protein 2 binds adenine nucleotides. *J. Biol. Chem.* 283, 20628–20634. doi:10.1074/jbc.M800738200